SEGMENTED PARALLEL AND SLANT-HOLE STATIONARY CARDIAC SINGLE PHOTON EMISSION COMPUTED TOMOGRAPHY

by

Yanfei Mao

A dissertation submitted to the faculty of
The University of Utah
in partial fulfillment of the requirements for the degree of

Doctor of Philosophy

Department of Bioengineering

The University of Utah

May 2015

The University of Utah Graduate School

STATEMENT OF DISSERTATION APPROVAL

The dissertation of   **Yanfei Mao**

has been approved by the following supervisory committee members:

Gengsheng L. Zeng	, Chair	**01/26/2015** Date Approved
Frederic Noo	, Member	**01/26/2015** Date Approved
Dennis L. Parker	, Member	**01/08/2015** Date Approved
Richard Rabbitt	, Member	**01/08/2015** Date Approved
Robert MacLeod	, Member	**01/08/2015** Date Approved

and by   **Patrick A. Tresco**   , Chair/Dean of

the Department/College/School of   **Bioengineering**

and by David B. Kieda, Dean of The Graduate School.

ABSTRACT

Single Photon Emission Computed Tomography (SPECT) myocardial perfusion imaging (MPI), a noninvasive and effective method for diagnosing coronary artery disease (CAD), is the most commonly performed SPECT procedure. Hence, it is not surprising that there is a tremendous market need for dedicated cardiac SPECT scanners. In this dissertation, a novel dedicated stationary cardiac SPECT system that using a segmented-parallel-hole collimator is investigated in detail. This stationary SPECT system can acquire true dynamic SPECT images and is inexpensive to build.

A segmented-parallel-hole collimator was designed to fit the existing general-purpose SPECT cameras without any mechanical modifications of the scanner while providing higher detection sensitivity. With a segmented-parallel-hole collimator, each detector was segmented to seven sub-detector regions, providing seven projections simultaneously. Fourteen view-angles over 180° were obtained in total with two detectors positioned at 90° apart. The whole system was able to provide an approximate 34-fold gain in sensitivity over the conventional single-head SPECT system.

The potential drawbacks of the stationary cardiac SPECT system are data truncation from small field of view (FOV) and limited number of view angles. A tailored maximum-likelihood expectation-maximization (ML-EM) algorithm was derived for reconstruction of truncated projections with few view angles. The artifacts caused by truncation and insufficient number of views were suppressed by reducing the image updating step sizes of the pixels outside the FOV. The performance of the tailored ML-EM algorithm was verified by computer simulations and phantom experiments. Compared with the conventional ML-EM algorithm, the tailored ML-EM algorithm successfully suppresses the streak artifacts outside the FOV and reduces the distortion inside the FOV. At 10 views, the tailored ML-EM algorithm has a much lower mean squared error (MSE) and higher relative contrast.

In addition, special attention was given to handle the zero-valued projections in the image reconstruction. There are two categories of zero values in the projection data: one is outside the boundary of the object and the other is inside the object region, which is caused by count starvation. A positive weighting factor c was introduced to the ML-EM

algorithm. By setting $c > 1$ for zero values outside the projection, the boundary in the image is well preserved even at extremely low iterations. The black lines, caused by the zero values inside the object region, are completely removed by setting $0 \leq c < 1$.

Finally, the segmented-parallel-hole collimator was fabricated and calibrated using a point source. Closed-form explicit expressions for the slant angles and rotation radius were derived from the proposed system geometry. The geometric parameters were estimated independently or jointly. Monte Carlo simulations and real emission data were used to evaluate the proposed calibration method and the stationary cardiac system. The simulation results show that the difference between the estimated and the actual value is less than $0.1°$ for the slant angles and the 5 mm for the rotation radius, which is well below the detector's intrinsic resolution.

CONTENTS

LIST OF FIGURES

LIST OF TABLES

ACKNOWLEDGMENTS

I owe an enormous debt to my doctoral supervisor, Prof. Gengsheng Lawrence Zeng. Larry is erudite and well known in the field of medical image reconstruction. His passion in teaching and research have strongly influenced me ever since we first met. During my long PhD journey, Larry has been continuously providing guidance, support, and encouragement. I have been most fortunate to be a student of Larry.

I am deeply grateful to my doctoral dissertation committee: Prof. Frédéric Noo, Prof. Dennis L. Parker, Prof. Richard D. Rabbitt, and Prof. Rob S. MacLeod. I appreciate your kind support and general advice on my doctoral research. I would also like to express my great gratitude to my colleagues at both the Utah Center of Advanced Imaging Research and at the Department of Bioengineering, for the pleasant time we spent during and off work. Finally, the most significant acknowledgement goes to my parents and husband, for their unconditional love and support.

CHAPTER 1

INTRODUCTION

1.1   Importance of Cardiac SPECT

Cardiovascular disease (CVD) is the leading cause of death in the U.S. for both men and women, killing 597,689 Americans in 2010—that is 1 in every 4 deaths [1, 2]. According to statistics released by the American Heart Association (AHA), over 84 million American adults suffer from CVD and on average 2,100 people die of CVD every day [3]. Early detection and risk assessment is key to preventing death. Single Photon Emission Computed Tomography (SPECT) imaging, presently considered state-of-the-art for myocardial perfusion imaging, involves injection of a small amount of radioactive tracers into the blood to produce accurate images of blood flow and perfusion. Myocardial perfusion imaging is performed in conjunction with either physical stress (exercise) or pharmacologic stress, identifying areas of relatively reduced blood flow in the myocardium associated with ischemia or scars. Unlike cardiovascular magnetic resonance imaging (MRI), cardiac SPECT is safe for patients with pacemakers and other metallic devices. In addition, it is much more affordable compared with myocardial positron emission tomography (PET) and cardiovascular MRI. Cardiac SPECT myocardial perfusion imaging has proven to be valuable in diagnosing, assessing, and evaluating treatment of CVD. It has been the most important imaging modality for coronary artery disease.

1.2   Cardiac SPECT Imaging

A typical cardiac SPECT scan involves three steps. Before the SPECT scan, the patient is injected with a chemical that is radiolabeled. These tracers mix with the blood and are taken up by living heart muscle. The gamma rays emitted from tracers are processed by a gamma camera, as shown in Figure 1.1. At the top of the camera is a collimator which is made of lead or tungsten. The lead walls, called septa, between the holes in the collimator absorb most photons and only those from nearly the same direction as the collimator holes can pass through the holes. These photons are further absorbed by a thallium-activated

Organ with radioactive emission

Collimator
NaI (Tl) crystal

Photomultiplier tubes (PMI)

Pre-amplifiers

Position decoding circuits
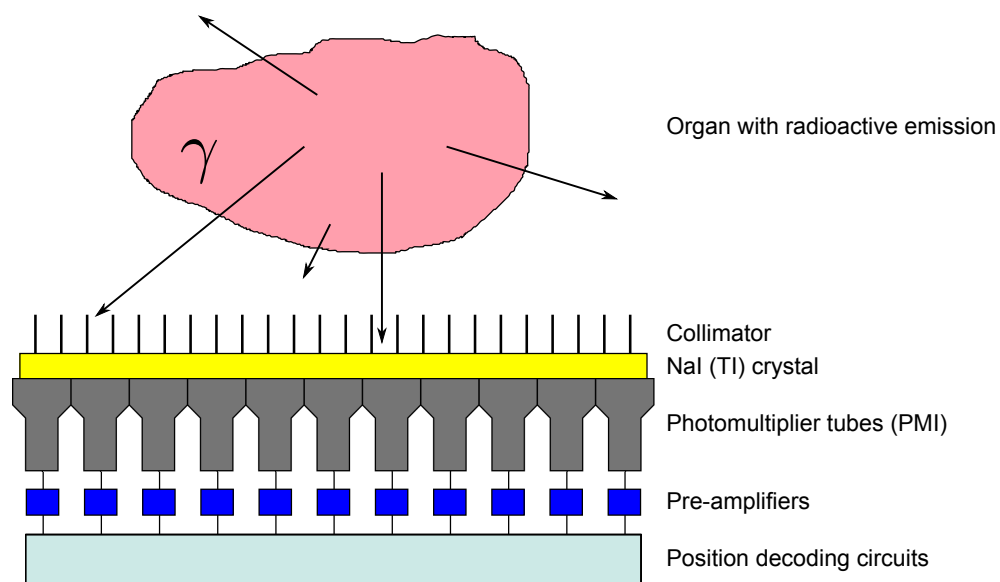
Figure 1.1: A SPECT camera head contains collimator, NaI(Tl) crystal, PMTs, pre-amplifier, and position decoding circuits.

sodium iodide [NaI(Tl)] crystal, typically 0.95 cm (3/8 inch) thick, causing the emission of visible light and ultraviolet (UV) radiation. A large number of 5.1- to 7.6-cm (2- to 3-inch) diameter photomultiplier tubes (PMTs) are coupled to the scintillator crystal to convert the light and UV photons into electrical signals and amplify the signals [4], which are further amplified by the preamplifiers. The position of each photon intersection in the crystal is determined by the relative amplitude of the pulse. The total energy deposited in the crystal produces the energy signal. Finally, the two-dimensional (2D) projections are converted into 3D images by reconstruction methods.

1.3   Weakness of Conventional SPECT System

The conventional SPECT system usually has two large cameras consisting of a NaI(TI) crystal with large photomultiplier tubes and parallel-hole collimators. The detectors collect the high-energy photons emitted by the patient and rotate 180° or 360° around the patient's body to provide a sufficient number of untruncated projections. However, in cardiac imaging, only a small portion of the detector area is used to image the heart, which leads to the system being inefficient (see Figure 1.2). In addition, dynamic SPECT studies are complicated in the rotation system because the radionuclide concentration in the field of view (FOV) changes over the time of acquisition for the different projections, resulting in inconsistent projection data.

1.4   Commercial Dedicated Cardiac SPECT

In an effort to overcome these limitations of the conventional SPECT system, several manufacturers recently developed innovatively designed dedicated cardiac SPECT systems with small FOV. The D-SPECT system, developed by Spectrum Dynamics, contains 10 sweeping parallel-beam detectors [5]. Digirad created a dedicated cardiac SPECT system that has stationary detectors and a rotating chair. The projections are collected by rotating the patient on the chair [6]. The CardiArc® scanner uses stationary curved detectors and a sweeping aperture arc with a series of vertical slots. The aperture arc rotates back and forth to provide enough view-angles and the horizontal vanes provide collimation in the axial direction [7]. All these three systems can be positioned very close to the patient to achieve high-sensitivity performance, but none of them are fully stationary. UC San Francisco and Western Cardiology Associates designed a stationary cardiac SPECT system using a multipinhole technique [8, 9]. Another newly developed stationary cardiac scanner is GE Healthcare's Discovery NM 530c®, which uses Alcyone technology, consisting of an array of CZT detectors and focused multipinhole collimators. With the multipinhole
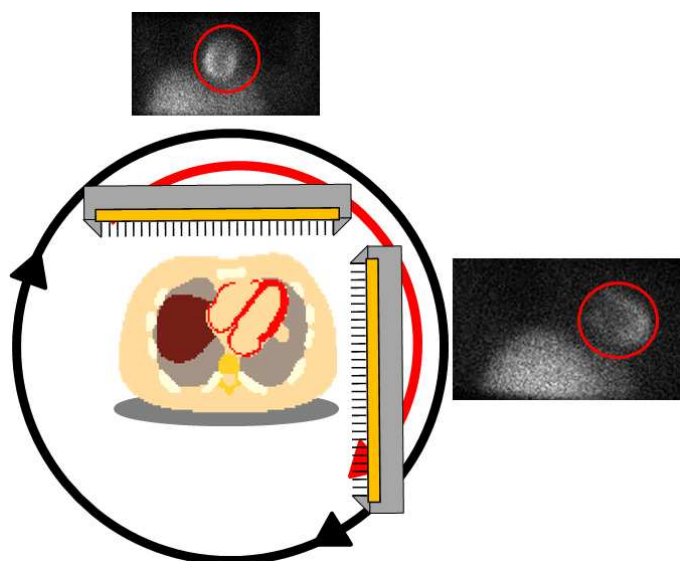
Figure 1.2: In the conventional SPECT system, only a small portion of the detectors are used for imaging the heart.

collimators, the scanner can simultaneously image all views with no moving parts during data acquisition [10, 11]. However, the image sensitivity is reduced as the multipinhole collimator operates in minification mode for human cardiac studies.

1.5 Pinhole vs. Parallel-hole

In this dissertation, a stationary cardiac SPECT system using a novel segmented slant-hole collimator has been investigated. This system is completely stationary during acquisition and is ideal for dynamic cardiac imaging.

The detection resolution and sensitivity of pinhole and parallel-hole were compared before collimator design. Collimator resolution and efficiency are usually used to describe the performance of the collimator. Collimator resolution R is defined as the full width at half maximum (FWHM) of the radiation profile of a point source projected on the detector through the collimator. Collimator efficient g is defined as the fraction of γ rays passing through the collimator per γ ray emitted by the source. Equations for collimator resolution (R_{ph}, R_{par}) and collimator efficiency (g_{ph}, g_{par}) for pinhole and parallel-hole collimators are given by [12]:

Pinhole Collimator:

$$R_{ph} \approx d_{ph}(f_{ph} + b_{ph})/f_{ph} \tag{1.1}$$

$$g_{ph} \approx d_{ph}^2/(16b_{ph}^2), \tag{1.2}$$

where f_{ph} is the focal-length of the pinhole. b_{ph} and d_{ph} represent the object-to-pinhole distance and the pinhole size, respectively.

Parallel-hole Collimator:

$$R_{par} \approx d_{par}(L + B)/L \tag{1.3}$$

$$g_{par} \approx K^2(d_{par}/L)^2, \tag{1.4}$$

where L indicates the hole length and B is the object-to-parallel-hole distance. K is a constant that depends on the hole shape (0.24 for round holes and 0.26 for hexagonal holes) and d_{par} represents the hole size. Here, we assume $K = 0.25$. The septal thickness and the penetration of gamma rays are not considered in the theoretical comparison part. For a fair comparison of the multipinhole collimator and segmented parallel-hole collimator, we assume these two systems have the same magnification factor and the object is placed at the same distance, that is, $f_{ph} = b_{ph} = B$ (see Figure 1.3).
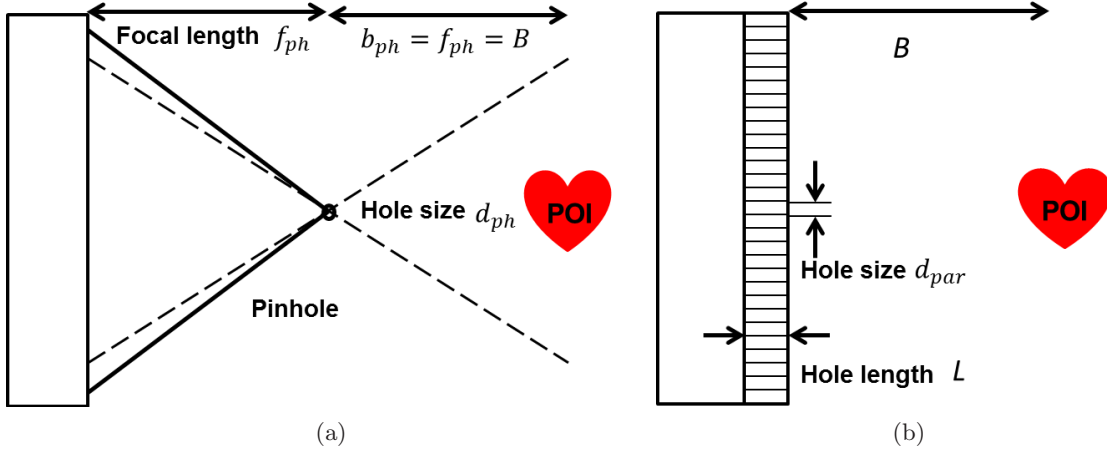
Figure 1.3: Parameters in pinhole and parallel-hole systems. (a) Parameters in a pinhole system. (b) Parameters in a parallel-hole system.

1.5.1 Detection Sensitivity Comparison at Equal Resolution

For equal resolution that $R_{ph} = R_{par}$, we can easily get $L_R = L = B/(2\beta - 1)$, where $\beta = d_{ph}/d_{par}$, from Equation 1.1 and 1.3. When $L = B/(2\beta - 1)$, the detector sensitivity ratio of both systems is given by

$$g_{par}/g_{ph} = (2 - 1/\beta)^2. \tag{1.5}$$

Because $\beta = d_{ph}/d_{par}$ is always larger than 1 in practice, $g_{par}/g_{ph} = (2 - 1/\beta)^2 > 1$, which means the parallel-hole collimator has better sensitivity.

1.5.2 Image Resolution Comparison at Equal Sensitivity

For equal sensitivity that $g_{ph} = g_{par}$, the parallel hole length $L_S = L = B/\beta$ according to Equation 1.2 and 1.4. Substituting this value for L in Equation 1.1 and 1.3, we can get the resolution ratio of two systems as

$$R_{par}/R_{ph} = (L + B)/(2\beta L) = 1/2 + 1/(2\beta). \tag{1.6}$$

When $\beta > 1$, which is always satisfied, $R_{par}/R_{ph} < 1$. As a consequence, the parallel-hole system has higher resolution than the pinhole system.

From the two comparisons above, we can see that the parallel-hole system outperforms the pinhole system in both resolution and sensitivity as long as the parallel-hole length is in the range of $L_R < L < L_S$, which is equivalent to $B/(2\beta - 1) < B/\beta$. This condition is always satisfied as $\beta > 1$.

1.6   Some Potential Concerns of Stationary Cardiac SPECT Systems

In a dedicated cardiac SPECT system, all detectors are constrained to image just the heart to ensure low cost and high efficiency. The potential drawback of a small FOV is that the background and other organs around the heart are truncated when they are not seen by all views. Another consideration of a stationary system is the lack of sufficient view-angles. These two problems were carefully studied in the design of the stationary cardiac SPECT system. In addition, a tailored Maximum-Likelihood Expectation-Maximization (ML-EM) algorithm has been developed for image reconstruction of truncated projections with limited number of views.

1.7   The Organization of the Dissertation

This dissertation focuses on stationary cardiac SPECT system design, image reconstruction problems in small FOV, and calibration approaches specific to the proposed system. There are six chapters in this dissertation, including this introductory chapter. In Chapter 2, a segmented slant-hole collimator is designed for a stationary cardiac SPECT system. A completely stationary cardiac SPECT system can acquire all projections simultaneously and is ideal for dynamic cardiac imaging. The multipinhole technique is widely used in current stationary SPECT systems [8–11, 13, 14]. In small animal SPECT, multipinhole collimation can provide high-sensitivity and high-resolution images for operating in the pinhole magnification mode [15], where the distance between the detector and the pinhole is larger than the distance between the pinhole and the object. However, for human cardiac studies, the multipinhole system operates in image reducing (instead of magnifying) mode, that is, the cardiac image is smaller than the heart. The detection sensitivity is reduced as a result. When the pinhole magnification factor is less than 1, the pinhole detection sensitivity becomes worse than that of a parallel-hole system. In this situation, the parallel-hole collimator outperforms the pinhole in detection sensitivity. So, we use a segmented slant-hole collimator in place of the multipinhole collimator to provide greater detection sensitivity. With segmented slant-hole collimators and two detectors, 14 views are acquired simultaneously. The Monte Carlo simulation results show that the proposed segmented slant-hole stationary cardiac SPECT system is able to acquire sufficient data for cardiac imaging and has very high sensitivity gain.

Chapter 3 presents a tailored Maximum-Likelihood Expectation-Maximization (ML-EM) algorithm for reconstruction of truncated projection data at small number of views. In dedicated stationary cardiac SPECT systems, the FOV is usually small and barely covers

the heart [10, 11, 16]. As a result, the background and other organs are severely truncated. Another potential drawback is the lack of sufficient number of views. Both drawbacks cause part of the object outside the FOV not to be fully scanned by the detector. The ML-EM algorithm [17, 18] is commonly used in emission tomography for image reconstruction. It has advantages of accurately modeling the imaging geometries, physics effects, and Poisson noise. When the projection data are not truncated, it is robust against noise and systematic inconsistencies. However, when the data are truncated and the view-angles are not sufficient at the same time, some image pixels outside the FOV diverge to extremely large values after a certain number of iterations, resulting in highly distorted reconstruction within the FOV. In order to suppress the artifacts caused by data truncation and insufficient angular sampling, a tailored ML-EM algorithm is introduced by reducing the image updating step sizes for the pixels outside the FOV. As a result, the reconstruction is more stabilized and the streak artifacts and distortion are suppressed.

In Chapter 4, a positive constant weighting factor c is introduced to zero-valued projections in the ML-EM algorithm. Recently, high-speed acquisition and dynamic studies are usually performed in cardiac imaging, generating low count data. When the measured count is very low, there is a probability that a zero-valued projection is measured. It may also happen when a preprocessing method, such as scatter correction, is applied. The zero measurement is correct if the projection ray does not pass through the radiation source body and it is most likely incorrect if the projection ray passes through the body. The wrong zero-measurement projections cause the black lines in the reconstruction when the ML-EM algorithm $c > 1$, so that the pixels in the background converge to 0 quickly and the boundary of the heart phantom is accurately reconstructed at low iterations. For zero values inside the projection of the radiation body, we de-emphasize the zero measurement by setting weighting factor $c < 1$. Without any correction, the ML-EM results show black lines due to the zero-values inside the object projection. With a change of the c value to a very small number that is less than 1, the black lines are completely removed.

In order to achieve accurate image reconstruction, a geometric calibration of the segmented slant-hole SPECT system is necessary. In the past thirty years, many calibration methods using one or multiple point sources have been proposed for parallel, fan-beam, cone-beam, and pinhole geometries [19–26]. In Chapter 5, a specific calibration method has been developed to estimate the geometric parameters of the segment slant-hole collimator used in the stationary cardiac SPECT system. The segmented slant-hole collimator includes seven sub-collimators slanted towards a common volume at the rotation center. The

parameters are first estimated independently from each section and further improved by a joint objective function that uses all collimator sections. The proposed calibration method was validated by Monte Carlo simulations and was implemented to a prototype stationary cardiac SPECT system.

Summary of the main contributions of this dissertation and some suggestions for future work are given in Chapter 6.

1.8   References

[1] "http://www.cdc.gov/nchs/fastats/lcod.htm," Sep. 23, 2013.

[2] "http://www.cdc.gov/heartdisease/facts.htm," Sep. 23, 2013.

[3] "http://www.heart.org/idc/groups/heart-public/@wcm/@adv/documents/ downloadable/ucm_304822.pdf," Jul. 12, 2011.

[4] J. T. Bushberg and J. M. Boone, *The essential physics of medical imaging.* Lippincott Williams & Wilkins, 2011.

[5] J. Patton, M. Sandler, D. Berman, S. Vallabhajosula, D. Dickman, S. Gambhir, *et al.*, "D-SPECT: a new solid state camera for high speed molecular imaging," *J. Nucl. Med.*, vol. 47, no. suppl 1, p. 189P, 2006.

[6] "http://www.digirad.com," Sep. 23, 2013.

[7] "http://cardiarc.com," Sep. 23, 2013.

[8] T. Funk, D. L. Kirch, J. E. Koss, E. Botvinick, and B. H. Hasegawa, "A novel approach to multipinhole SPECT for myocardial perfusion imaging," *J. Nucl. Med.*, vol. 47, no. 4, pp. 595–602, 2006.

[9] P. P. Steele, D. L. Kirch, and J. E. Koss, "Comparison of simultaneous dual-isotope multipinhole SPECT with rotational SPECT in a group of patients with coronary artery disease," *J. Nucl. Med.*, vol. 49, no. 7, pp. 1080–1089, 2008.

[10] F. P. Esteves, P. Raggi, R. D. Folks, Z. Keidar, J. Wells Askew, S. Rispler, M. K. OConnor, L. Verdes, and E. V. Garcia, "Novel solid-state-detector dedicated cardiac camera for fast myocardial perfusion imaging: multicenter comparison with standard dual detector cameras," *J. Nucl. Cardiol.*, vol. 16, no. 6, pp. 927–934, 2009.

[11] M. Bocher, I. M. Blevis, L. Tsukerman, Y. Shrem, G. Kovalski, and L. Volokh, "A fast cardiac gamma camera with dynamic SPECT capabilities: design, system validation and future potential," *Eur. J. Nucl. Med. Mol. Imag.*, vol. 37, no. 10, pp. 1887–1902, 2010.

[12] S. R. Cherry, J. A. Sorenson, and M. E. Phelps, *Phys. Nucl. Med.* Elsevier Health Sciences, 2012.

[13] Z. Liu, G. A. Kastis, G. D. Stevenson, H. H. Barrett, *et al.*, "Quantitative analysis of

acute myocardial infarct in rat hearts with ischemia-reperfusion using a high-resolution stationary SPECT system," *J. Nucl. Med.*, vol. 43, no. 7, pp. 933–939, 2002.

[14] F. J. Beekman and B. Vastenhouw, "Design and simulation of a high-resolution stationary SPECT system for small animals," *Phys. Med. Biol.*, vol. 49, pp. 4579–4592, 2004.

[15] N. U. Schramm, G. Ebel, U. Engeland, T. Schurrat, M. Behe, and T. M. Behr, "High-resolution SPECT using multipinhole collimation," *IEEE Trans. Nucl. Sci.*, vol. 50, no. 3, pp. 315–320, 2003.

[16] E. Garcia and T. Faber, "New trends in camera and software technology in nuclear cardiology," *Cardiol. Clin.*, vol. 27, no. 2, pp. 227–236, 2009.

[17] L. Shepp and Y. Vardi, "Maximum likelihood reconstruction for emission tomography," *IEEE Trans. Med. Imaging*, vol. 1, no. 2, pp. 113–122, 1982.

[18] K. Lange, R. Carson, *et al.*, "EM reconstruction algorithms for emission and transmission tomography," *J. Comput. Assist. Tomogr.*, vol. 8, no. 2, pp. 306–316, 1984.

[19] E. Busemann-Sokole, "Measurement of collimator hole angulation and camera head tilt for slant and parallel hole collimators used in SPECT," *J. Nucl. Med.*, vol. 28, no. 10, pp. 1592–1598, 1987.

[20] G. Gullberg, B. Tsui, C. Crawford, and E. Edgerton, "Estimation of geometrical parameters for fan beam tomography," *Phys. Med. Biol.*, vol. 32, no. 12, pp. 1581–1594, 1987.

[21] G. Gullberg, B. Tsui, C. Crawford, J. Ballard, and J. Hagius, "Estimation of geometrical parameters and collimator evaluation for cone beam tomography," *Med. Phys.*, vol. 17, no. 2, pp. 264–272, 1990.

[22] Y. Hsieh, G. Zeng, G. Gullberg, and H. Morgan, "A method for estimating the parameters of a fan-beam and cone-beam SPECT system using five point sources," *J. Nucl. Med.*, vol. 34, no. 5, pp. 191–191, 1993.

[23] P. Rizo, P. Grangeat, and R. Guillemaud, "Geometric calibration method for multiple-head cone-beam SPECT system," *IEEE Trans. Nucl. Sci.*, vol. 41, no. 6, pp. 2748–2757, 1994.

[24] F. Noo, R. Clackdoyle, C. Mennessier, T. A. White, and T. J. Roney, "Analytic method based on identification of ellipse parameters for scanner calibration in cone-beam tomography," *Phys. Med. Biol.*, vol. 45, no. 11, p. 3489, 2000.

[25] D. Bequé, J. Nuyts, G. Bormans, P. Suetens, and P. Dupont, "Characterization of pinhole spect acquisition geometry," *IEEE Trans. Med. Imaging*, vol. 22, no. 5, pp. 599–612, 2003.

[26] D. Bequé, J. Nuyts, P. Suetens, and G. Bormans, "Optimization of geometrical calibration in pinhole spect," *IEEE Trans. Med. Imaging*, vol. 24, no. 2, pp. 180–190, 2005.

CHAPTER 2

SEGMENTED SLANT-HOLE COLLIMATOR
FOR STATIONARY CARDIAC SPECT:
THE MONTE CARLO SIMULATIONS

2.1 Abstract

This work is preliminary to the design of a stationary cardiac SPECT system. The goal of this research is to propose a stationary cardiac SPECT system using segmented slant-hole collimators and to perform some computer simulations to test the feasibility. Compared to the rotational SPECT, a stationary system has a benefit of acquiring temporally consistent projections. The most challenging issue in building a stationary system is to provide sufficient projection view-angles.

A GATE (Geant4 Application for Tomographic Emission) Monte Carlo model was developed to simulate the two-detector stationary cardiac SPECT that uses segmented slant-hole collimators. Each detector contains seven segmented slant-hole sections that slant to a common volume at the rotation center. Consequently, 14 view-angles over 180° were acquired without any gantry rotation. The NCAT phantom was used for data generation and the tailored maximum-likelihood expectation-maximization (ML-EM) algorithm was used for image reconstruction. Effects of limited number of view-angles and data truncation were carefully evaluated in the paper.

Simulation results indicated that the proposed segmented slant-hole stationary cardiac SPECT system is able to acquire sufficient data for cardiac imaging without a loss of image quality. A short hole-length not only reduces the dead-zone between two sub-collimators, but also increases detector sensitivity. The measured sensitivity gain is about 34-fold over the conventional single-head system.

The GATE Monte Carlo simulations confirm the feasibility of the proposed stationary cardiac SPECT system with segmented slant-hole collimators. The proposed collimator consists of combined parallel and slant holes, and the image on the detector is not reduced in size.

2.2   Introduction

The growth of cardiovascular disease (CAD), which is a leading cause of death and morbidity worldwide, has created an urgent need for an efficient, noninvasive tool. Among current diagnostic methods, Single Photon Emission Computed Tomography (SPECT), in particular SPECT myocardial perfusion imaging (MPI), remains the most important and efficient method for diagnosing coronary artery disease noninvasively.

In the past decade, several high-speed cardiac SPECT systems have been developed, *e.g.*, D-SPECT (Spectrum Dynamics, Caesarea, Israel) [1, 2], Cardius 3 XPO (Digirad, Poway, CA) [3], and CardiArc (CardiArc, Lubbock, TX) [2, 4]. In comparison with the conventional SPECT system, dedicated cardiac SPECT permits fast acquisition of high sensitivity and quality images, facilitating the process of dynamic cardiac imaging. The usage of novel photon-collection and scanning geometries increases the detector efficiency significantly, but the detector motion or the slit motion in current cardiac systems leads to data inconsistencies between views, as do conventional rotational SPECT systems.

To create a stationary system, the multipinhole technique, which is the state-of-the-art in small animal imaging, has been extended to human cardiac SPECT [5–10]. With the main advantage being the pinhole magnification effect (Figure 2.1a), it allows a high-sensitivity, high-resolution image to be obtained in small animal imaging [11]. However, for human cardiac studies, the multipinhole system operates in minification mode, that is, the object is placed away from the pinhole and the images on the detector are smaller than the object (Figure 2.1b) *e.g.*, UC San Francisco and Western Cardiology Associate's stationary multipinhole system [7, 8, 12], Discovery NM 530c (GE Healthcare, Haifa, Israel) [9, 10]. The detection sensitivity thus decreases dramatically, even more than that for a parallel-hole collimator when the object is far away from the pinhole. In this situation, the parallel-hole collimator outperforms the pinhole in detection sensitivity for human cardiac SPECT.

We therefore have investigated a novel dedicated stationary cardiac SPECT system with segmented slant-hole collimators, to provide greater detection sensitivity over the multipinhole cardiac SPECT system. The segmented slant-hole collimator, which is designed to fit existing dual-head SPECT cameras, includes seven sub-collimators. During data acquisition, our novel system is completely stationary and 14 views in total are acquired simultaneously. Detailed computer simulation results of the whole system are presented and compared with that of the conventional SPECT system.
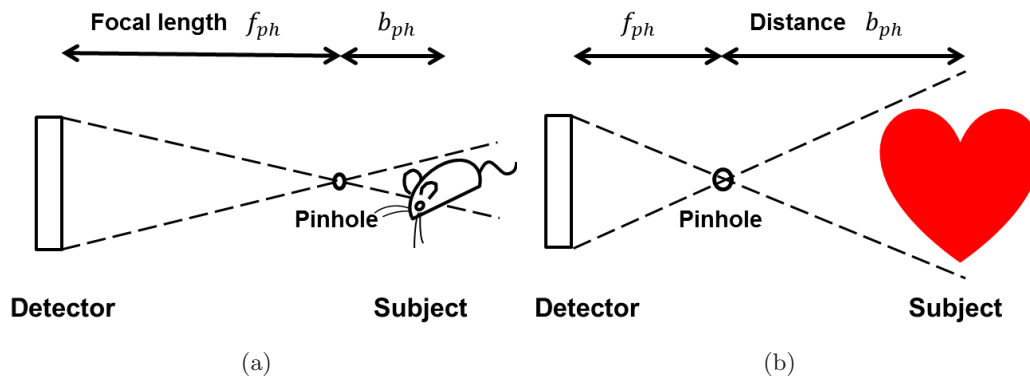
Figure 2.1: Pinhole collimation. Left: For small animal cardiac studies, the pinhole operates at magnification mode. Right: For human cardiac studies, the pinhole works in image reducing mode.

2.3 Design and Methods

2.3.1 Imaging Configuration and Modification

To take advantage of the existing dual-detector system and lower the cost of a stationary cardiac SPECT system, our strategy is to redesign the collimator for the conventional SPECT system to acquire projections at more view angles for each detector position. In UC San Francisco's stationary multipinhole system, a 3×3 configuration, as shown in Figure 2.2a, is used [7]. Although the 3×3 configuration has 9 pinholes in total, it only provides 3 view-angles in the horizontal (*i.e.*, transaxial) direction and 3 view-angles in the vertical (*i.e.*, axial) direction. Similarly, GE's Discovery NM 530c (DNM), which has 19 pinholes configured in the 3×9 format, only provides 9 independent views in the transaxial direction [10, 13]. However, a slight shift of the pinholes' position can provide more view-angles in the horizontal plane, which is perpendicular to the rotation axis. In Figure 2.2b, we see that view-angles are staggered in the horizontal plane by shifting the top row of pinholes to the left and the bottom row of pinholes to the right, providing 7 different view-angles in the horizontal plane. The view-angles in the horizontal direction provide the main contribution for image reconstruction. This modified approach increases the number of independent view-angles in the transaxial direction and is extended to the design of the segmented parallel-hole collimator (as seen in Figure 2.2c). The projection data acquired from the anterior to left anterior oblique (LAO) aspects of the patient's body have lower attenuation to the heart while the signal-to-noise ratio is relatively high. Accordingly, in our design, two detectors are positioned in an L-configuration (Figure 2.3), making it possible to acquire data by all segments over 180° from the LAO direction.

2.3.2 Collimator Designs

Our primary concern at this stage is the optimization of the collimator segment angles. The distance from the rotation center to the surface of the detector and the slant angle are chosen to minimize the overlap of the projections, maximize the acquisition angle (180°), and avoid out-of-boundary truncation of the projections in the region of interest (ROI). According to surveys of patient sizes and heart dimensions in a relatively large population [14–16], the size of the heart does not change very much between male and female, nor between small patients and large patients. Therefore, it is possible to design a collimator that fits all patients. In our system, the central-field-of-view (CFOV) is set at 12 cm in diameter which is large enough to cover the left ventricle.

We assume the heart is contained in a sphere positioned in front of the CFOV and is seen by all sub-detectors simultaneously. Its projection is a circle at the central sub-detector and
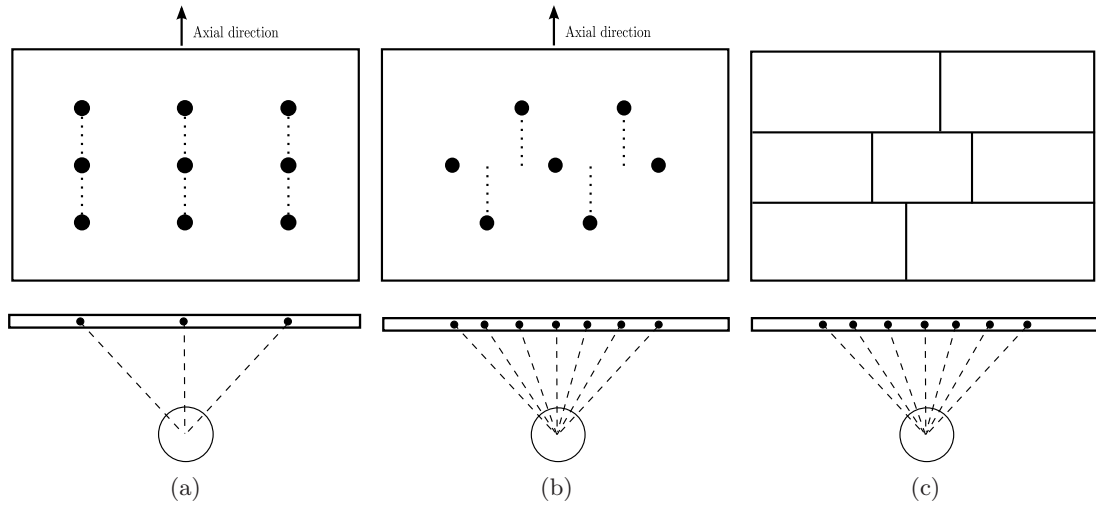
Figure 2.2: Image configuration and the view-angles in the horizontal direction. (a) UC San Francisco's 3×3 pinhole configuration of their pinhole system. (b) A revised, shifted 2-3-2 configuration. (c) The 2-3-2 configuration is used in the segmented parallel-hole collimator.
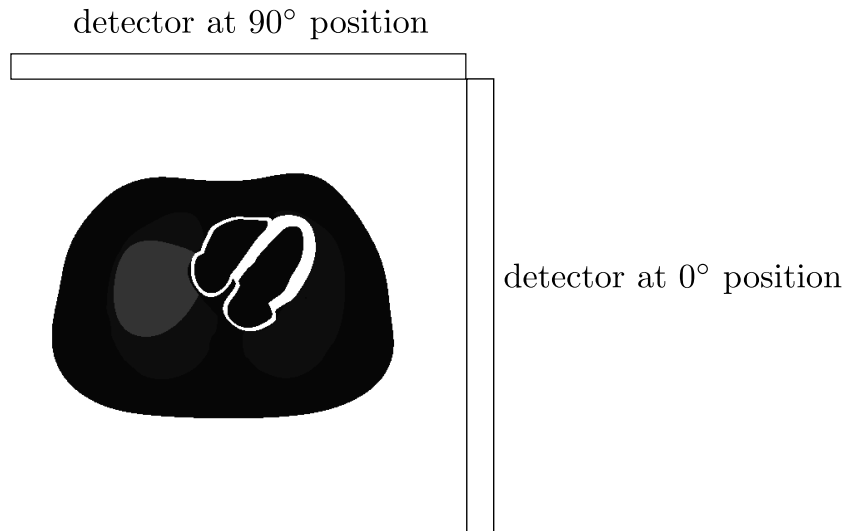
Figure 2.3: Two detectors are in an L-configuration.

an ellipse at the outer position (see Figure 2.4). Parameters are illustrated in Table 2.1. Each detector should cover 90° to get the 180° full coverage by two detectors. There are seven sub-detection regions in each detector, thus, the angular sampling interval $\theta=90°/7=12.9°$. In order to perform the L-configuration, the rotation radius F is chosen as half of the detector length, this is $F=53.3/2=26.65$ cm. Each slant angle η is determined according to Figure 2.5a. As seen in Figure 2.5a and 2.5b, the slant angle is also limited by the detector size and must satisfy:

$$\frac{R}{\cos\varphi} + R \leq F\tan\varphi \tag{2.1}$$

$$\frac{R}{\cos\eta} + F\tan\eta \leq L/2. \tag{2.2}$$

That is, $\varphi \leq 25.3761°$ and $\eta \leq 35.8396°$.

Applying the restrictions, the slant angles η are set as -35°, -25.7°, -12.9°, 0°, 12.9°, 25.7°, 35°, respectively, and the corresponding angle φ are -6.1°, 22°, -24.5°, 0°, 24.5°, -22°, 6.1°, respectively. The second detector is the same as the first detector, so we only need to design one detector and apply it to another.
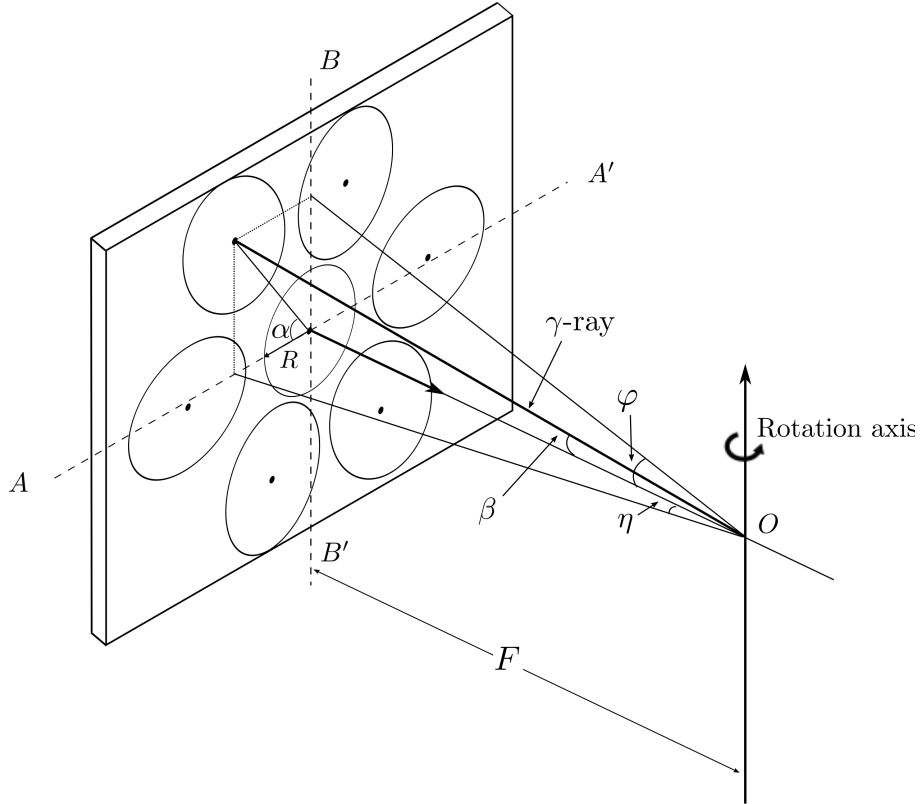
Figure 2.4: Definition of slant angles in segmented-slant-beam collimator.

Table 2.1: Defined geometric parameters of segmented-slant-beam collimator

Symbol	Description
α	angle between the horizontal (*i.e*, transaxial) axis and the major axis of the ellipse
β	angle between the detector norm and the γ-ray
φ	slant angle of γ-ray in the horizontal (*i.e.*, transaxial) direction, $\varphi \in (-90°, 90°)$
η	slant angle of γ-ray in vertical (*i.e.*, axial) direction, $\eta \in (-90°, 90°)$
L	detector length, L=53.3 cm
W	detector width, W=38.7 cm
R	radius of the central-field-of-view (CFOV)
F	distance from the rotation center to the detector
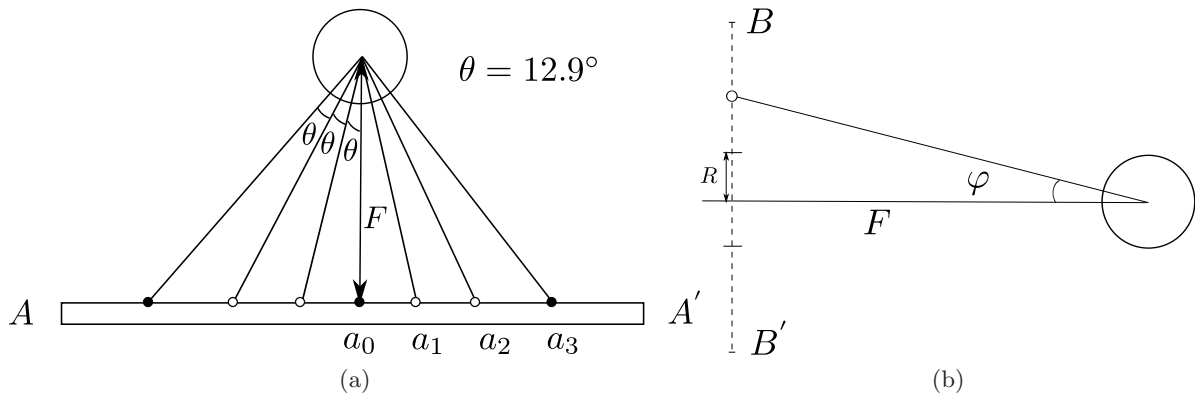
Figure 2.5: Calculate angles of the segmented-slant-hole collimator. (a) 7 views have an angular spacing of θ in the horizontal (*i.e.*, transaxial) direction. (b) The slant angle φ in the vertical direction.

2.3.3   Using Curved Segment Boundaries to Fit Images in the Detector

Unlike the parallel-hole collimator, the projections of the object are consequently elongated in the direction of slant. More detector space is therefore required in the direction of the slant for collimators at outer positions. The configuration in Figure 2.2c is thus not very efficient and may cause out-of-boundary truncation in the vertical direction. Our modification is to replace some straight-line boundaries of the sub-collimators (Figure 2.2c) with curved boundaries, as shown in Figure 2.6. The central sub-detector is round and has the most important tomographic information, so we must guarantee there is no truncation to the heart in this region. The curved boundaries follow the projection boundaries of the sphere and are large enough to cover the whole heart.

2.3.4   Using a Thin Collimator to Reduce the Detector Dead Zones

The disadvantage of the segmented parallel-hole collimator is the dead zone between two sub-collimators, as shown in Figure 2.7 (left). The dead area, which is not used for data acquisition, is defined by the slant angle and the hole length. Thus, we use a very thin collimator to reduce the detector dead zone as much as possible (Figure 2.7 right). A short hole length also allows more photons to be acquired by the detector, which increases the detector sensitivity. Our previous research has shown that an image reconstructed from a high-sensitivity collimator is less noisy than that from a high-resolution collimator and with collimator-blurring compensation, the high-sensitivity image can have comparable resolution to the high-resolution image [17].

2.4   Evaluation of Collimator

2.4.1   Theoretical Estimation of Total Sensitivity Gain

Compared with the conventional parallel-hole detector, our detector can acquire 7 projections simultaneously. The sensitivity gain of the segmented slant-hole collimator over the conventional parallel-hole collimator:

$$1 + 2\sum_{i=1}^{3} \cos^3 \beta_i = 1 + 2\sum_{i=1}^{3} \frac{1}{\left(\sqrt{\tan^2 \varphi_i + \tan^2 \eta_i + 1}\right)^3} = 4.7147. \qquad (2.3)$$

We have two detectors, so the total sensitivity of our proposed stationary segmented slant-hole system can have a 12-fold sensitivity gain over a conventional single-head system, if the collimators have the same resolution. In order to reduce the dead zone, the collimator
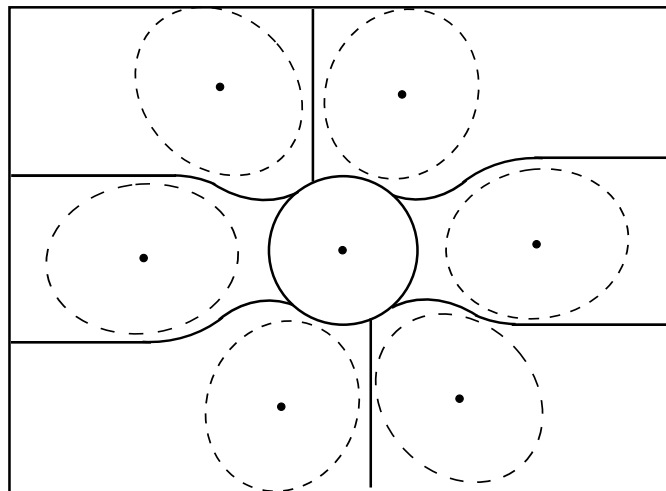
Figure 2.6: The detector is segmented into 7 sub-detection regions using curved boundaries. A spherical object is projected on the detector and 7 projections are obtained.
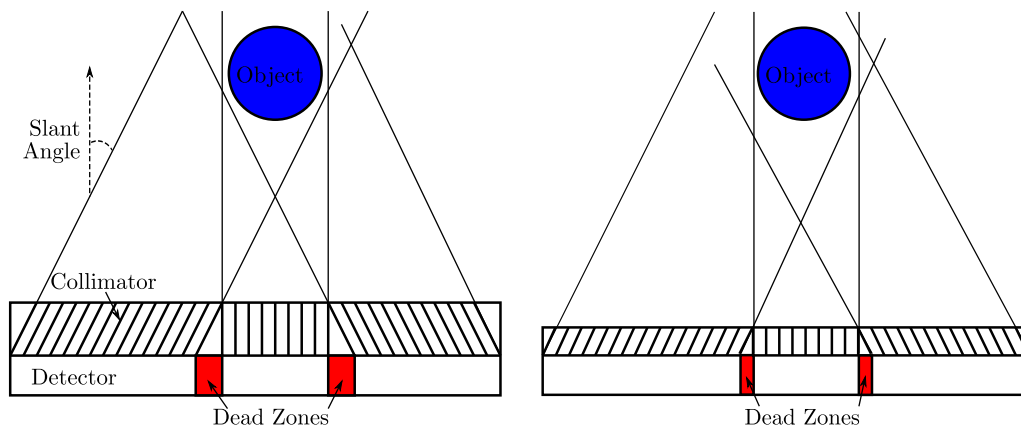
Figure 2.7: Left: large dead zones are observed between two sub-collimators. Right: dead zones are reduced with shorter hole length.

hole length is shortened, resulting in high-sensitivity collimators, and a 34-fold sensitivity gain over the conventional single-head system is measured from the prototype system.

2.4.2   Monte Carlo Simulation of the Stationary Cardiac System

A 3D numerical myocardial phantom (NCAT phantom) [18] and the GATE (Geant4 Application for Tomographic Emission) Monte Carlo simulation tool [19, 20], which include the effects of noise, attenuation, collimator-detector response, and scatter, were used for evaluating the segmented slant-hole collimator. The Monte Carlo code simulated the proposed stationary segmented slant-hole SPECT system as well as a conventional dual-head SPECT system, which has an FOV of 53.3×38.7 cm and a low-energy high-resolution (LEHR) collimator (hole length 24.05 mm and diameter 1.11 mm).

The gold-standard is the reconstruction from projections at 60 views uniformly spaced over 180° using a conventional rotational SPECT system. For a fair comparison, the total scan time and the system resolution were kept the same in both systems. The rotation radius equals 26.65 cm. Small FOV (12×12 cm) projections are obtained from full FOV projections by removing the pixels outside the small FOV. The projection data were acquired in 64×64 arrays with a pixel size of 6.25 cm. Images were reconstructed using a tailored maximum-likelihood expectation-maximization (ML-EM) algorithm [21]. In image reconstruction, collimator blurring was corrected and 35 iterations were applied.

The effects of truncation and number of view-angles are evaluated by using a visualization study, which identifies whether there are any artifacts and shape distortions in the reconstructed images. Three orthogonal cuts through the heart center were displayed. For further quantitative assessment, image profiles through the central slice of the reconstructed images were shown and compared with the conventional system.

2.5   Monte Carlo Simulation Results

The reconstruction results of the conventional SPECT system and the proposed stationary SPECT system are shown in Figure 2.8. In stationary segmented slant-hole SPECT, the heart has to be placed in the detector center, which is not required by the conventional SPECT. For equal comparison, the heart in the reconstruction of the conventional system was shifted to the image center and a similar slice was displayed. In order to study the effects of number of view angles, an image, which is reconstructed from the same angular sampling as the stationary system but without truncation, is also displayed. In comparison with the reconstruction results of 60 views, 14 views are sufficient to reconstruct the heart without any shape distortion. At the same scan time, the segmented slant-hole SPECT
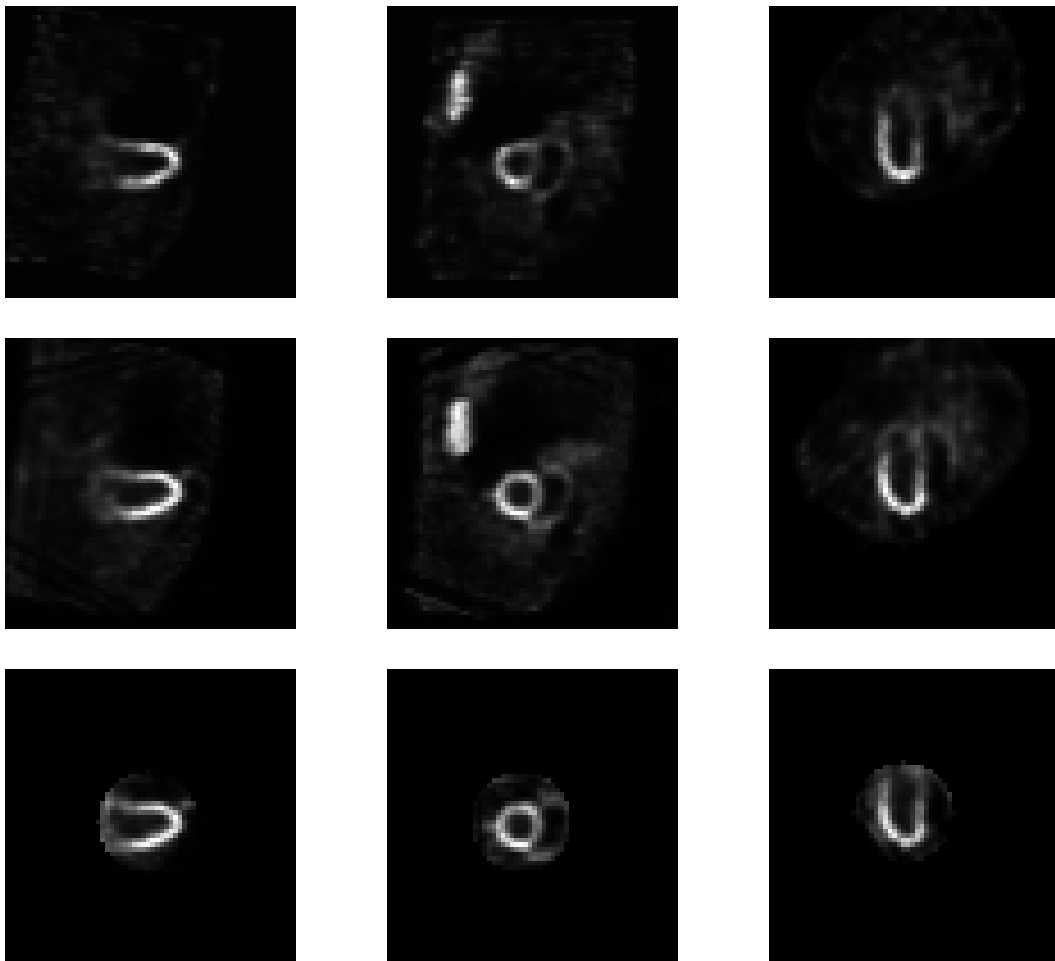
Figure 2.8: Reconstruction results of conventional SPECT and stationary segmented-slant-hole SPECT. From top to bottom: reconstruction results of the conventional SPECT at 60 views, the stationary segmented-slant-hole SPECT without and with truncation, respectively. 27 iterations were applied.

can acquire more photons than the conventional system, so the reconstructed image of the segmented slant-hole system is more uniform around the apex. When the projection data are truncated by the small FOV, the images overall are very well resolved, except for a slight loss of contrast.

Figure 2.9 compares the profile curves from the central column of the vertical long-axis, short-axis, and horizontal long-axis cuts, respectively. In the region of interest (ROI), the profile curves of the reconstruction from the segmented-slant-hole SPECT follow those from the conventional SPECT system quite well.

2.6   Discussion and Conclusions

We proposed a stationary cardiac SPECT system using segmented slant-hole collimators to acquire 14 views simultaneously. Each detector measures 7 views in the transaxial directions. It is very challenging to use a 53.3 cm × 38.7 cm detection area to measure 7 nonoverlapped heart images. Background data truncation problems cannot be avoided. Heart mispositioning can make the entire scan useless. The good news is that for a stationary imaging system, patient positioning is much easier than that in a rotational system. Once the heart is positioned in the center of the common FOV, the heart will stay there during the entire scan. Another good news is that the heart size seems to be unrelated to the patient body habitus, *e.g.*, the left ventricle diameter for a patient above 210 lbs is about 9 cm while it is 8∼10 cm for a patient below 186 lbs [16].

The Monte Carlo simulations show that the image reconstructed from the segmented slant-hole system has less noise than that from the conventional SPECT system at the same acquisition time and image resolution. The effect of truncation on the reconstructed image is slight and no distortion was observed. Therefore, our 14-view-angle, 2-detector, parallel-hole, stationary cardiac SPECT is able to measure sufficient data for cardiac imaging with a gain of image sensitivity.

The distance from the heart center to the detector may be too large and may cause a reduction of image resolution. In a further design, the patient will be positioned closer to the detector to get higher resolution. Accordingly, the detector will no longer be symmetrically segmented (as seen in Figure 2.10). The collimator on the detector at the 90° position in Figure 2.3 will have a mirror-reflection design of the collimator on the detector at 0° position.

2.7   Acknowledgments
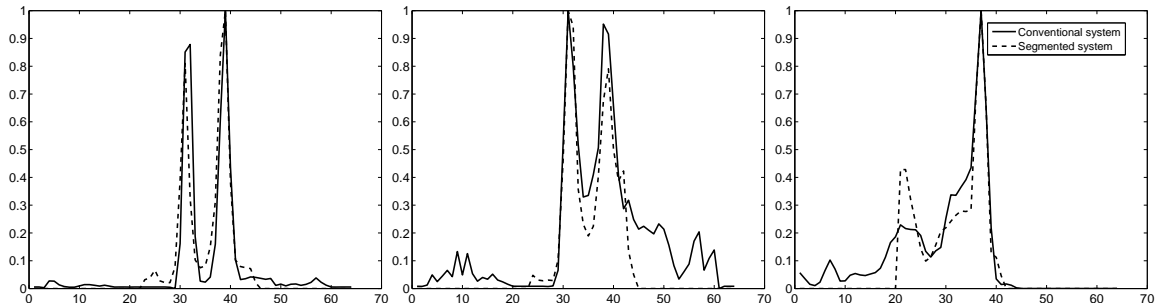
Figure 2.9: The profiles through the central column of each cut. From left to right: vertical long-axis, short-axis, and horizontal long-axis.
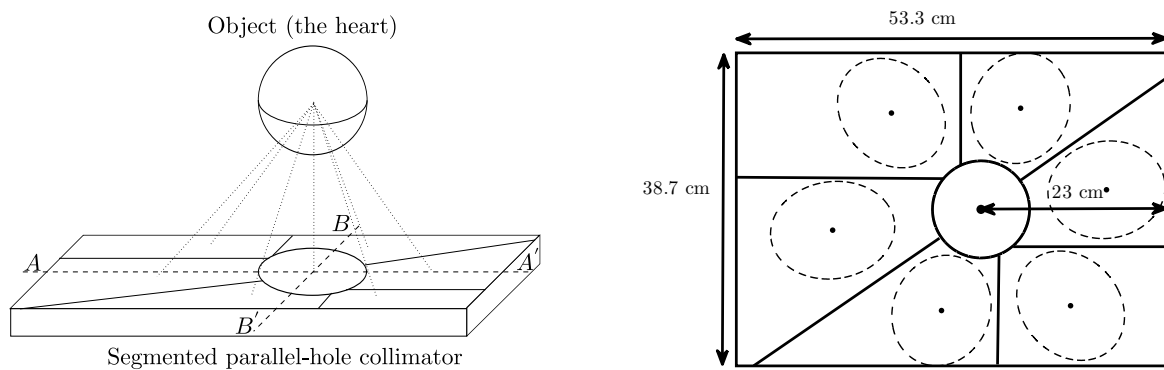
Figure 2.10: An asymmetric segmented-parallel-hole collimator.

2.8 References

[1] J. Patton, M. Sandler, D. Berman, S. Vallabhajosula, D. Dickman, S. Gambhir, *et al.*, "D-SPECT: a new solid state camera for high speed molecular imaging," *J. Nucl. Med.*, vol. 47, no. suppl 1, p. 189P, 2006.

[2] J. Patton, P. Slomka, G. Germano, and D. Berman, "Recent technologic advances in nuclear cardiology," *J. Nucl. Cardiol.*, vol. 14, no. 4, pp. 501–513, 2007.

[3] H. Babla, C. Bai, and R. Conwell, "A triple-head solid state camera for cardiac single photon emission tomography (SPECT)," in *Proceddings of SPIE*, vol. 6319, pp. 63190M–1–63190M–4, 2006.

[4] "http://cardiarc.com/cardiarc_scanner.html," Accessed April 23, 2012.

[5] Z. Liu, G. A. Kastis, G. D. Stevenson, H. H. Barrett, L. R. Furenlid, M. A. Kupinski, D. D. Patton, and D. W. Wilson, "Quantitative analysis of acute myocardial infarct in rat hearts with ischemia-reperfusion using a high-resolution stationary SPECT system," *J. Nucl. Med.*, vol. 43, no. 7, pp. 933–939, 2002.

[6] F. J. Beekman and B. Vastenhouw, "Design and simulation of a high-resolution stationary SPECT system for small animals," *Phys. Med. Biol.*, vol. 49, pp. 4579–4592, 2004.

[7] T. Funk, D. L. Kirch, J. E. Koss, E. Botvinick, and B. H. Hasegawa, "A novel approach to multipinhole SPECT for myocardial perfusion imaging," *J. Nucl. Med.*, vol. 47, no. 4, pp. 595–602, 2006.

[8] P. P. Steele, D. L. Kirch, and J. E. Koss, "Comparison of simultaneous dual-isotope multipinhole SPECT with rotational SPECT in a group of patients with coronary artery disease," *J. Nucl. Med.*, vol. 49, no. 7, pp. 1080–1089, 2008.

[9] F. P. Esteves, P. Raggi, R. D. Folks, Z. Keidar, J. Wells Askew, S. Rispler, M. K. OConnor, L. Verdes, and E. V. Garcia, "Novel solid-state-detector dedicated cardiac camera for fast myocardial perfusion imaging: multicenter comparison with standard dual detector cameras," *J. Nucl. Cardiol.*, vol. 16, no. 6, pp. 927–934, 2009.

[10] M. Bocher, I. Blevis, L. Tsukerman, Y. Shrem, G. Kovalski, and L. Volokh, "A fast cardiac gamma camera with dynamic SPECT capabilities: design, system validation and future potential," *Eur. J. Nucl. Med. Mol. Imag.*, vol. 37, no. 10, pp. 1887–1902, 2010.

[11] N. U. Schramm, G. Ebel, U. Engeland, T. Schurrat, M. Behe, and T. M. Behr, "High-resolution SPECT using multipinhole collimation," *IEEE Trans. Nucl. Sci.*, vol. 50, no. 3, pp. 315–320, 2003.

[12] J. D. Bowen, Q. Huang, J. R. Ellin, T. Lee, U. Shrestha, G. T. Gullberg, and Y. Seo, "Design and performance evaluation of a 20-aperture multipinhole collimator for myocardial perfusion imaging applications," *Phys. Med. Biol.*, vol. 58, no. 20, pp. 7209–7226, 2013.

[13] P. J. Slomka, D. S. Berman, and G. Germano, "New cardiac cameras: single-photon emission CT and PET," in *Seminars in Nuclear Medicine*, vol. 44, pp. 232–251, Elsevier, 2014.

[14] A. Oberman, A. R. Myers, T. M. Karunas, and F. H. Epstein, "Heart size of adults in a natural population-tecumseh, michigan variation by sex, age, height, and weight," *Circulation*, vol. 35, no. 4, pp. 724–733, 1967.

[15] A. B. Barclay, R. L. Eisner, and E. DiBella, "Construction of a thorax model database from clinical PET attenuation scans," in *Annual Meeting of the Society of Nuclear Medicine, Minneapolis, MN*, 1995.

[16] S. Devi, R. Clackdoyle, and P. Christian, "Torso and heart dimensions of cardiac SPECT patients," in *Conference Record 1997 Nuclear Science Symposium and Medical Imaging Conference, Albuquerque, NM*, vol. 2, pp. 1087–1091, IEEE, 1997.

[17] B. Zhang and G. L. Zeng, "High-resolution versus high-sensitivity SPECT imaging with geometric blurring compensation for various parallel-hole collimation geometries," *IEEE Trans. Inf. Technol. Biomed.*, vol. 14, no. 4, pp. 1121–1127, 2010.

[18] W. P. Segars, *Development of a new dynamic NURBS-based cardiac torso (NCAT) phantom.* PhD thesis, University of North Carolina, 2001.

[19] D. Strulab, G. Santin, D. Lazaro, V. Breton, and C. Morel, "GATE (Geant4 Application for Tomographic Emission): a PET/SPECT general-purpose simulation platform," *Nucl. Phys. B (Proc. Suppl.)*, vol. 125, pp. 75–79, 2003.

[20] S. Jan, G. Santin, D. Strul, S. Staelens, K. Assie, D. Autret, S. Avner, R. Barbier, M. Bardies, P. Bloomfield, *et al.*, "GATE: a simulation toolkit for PET and SPECT," *Phys. Med. Biol.*, vol. 49, no. 19, pp. 4543–4561, 2004.

[21] Y. Mao and G. L. Zeng, "A tailored ML-EM algorithm for reconstruction of truncated projection data using few view angles," *Phys. Med. Biol.*, vol. 58, no. 12, pp. N157–N169, 2013.

CHAPTER 3

A TAILORED ML-EM ALGORITHM FOR RECONSTRUCTION OF TRUNCATED PROJECTION DATA USING FEW VIEW-ANGLES

3.1   Abstract

Dedicated cardiac Single Photon Emission Computed Tomography (SPECT) systems have the advantage of high speed and sensitivity at no loss, or with even a gain, in resolution. The potential drawbacks of these dedicated systems are data truncation by the small field of view (FOV) and the lack of view-angles. Serious artifacts, including streaks outside the FOV and distortion in the FOV, are introduced to the reconstruction when using the traditional emission data Maximum-Likelihood Expectation-Maximization (ML-EM) algorithm to reconstruct images from the truncated data at small number of views. In this paper, we propose a tailored ML-EM algorithm to suppress the artifacts caused by data truncation and insufficient angular sampling by reducing the image updating step sizes for the pixels outside the FOV. As a consequence, the convergence speed for the pixels outside the FOV is decelerated. We applied the proposed algorithm to truncated analytical data, Monte Carlo simulation data, and real emission data at different numbers of views. The computer simulation results show that the tailored ML-EM algorithm outperforms the conventional ML-EM algorithm in terms of streak artifacts and distortion suppression for reconstruction from truncated projection data with a small number of views.

3.2   Introduction

Single Photon Emission Computed Tomography (SPECT) myocardial perfusion imaging is a noninvasive and effective method for diagnosing coronary artery disease. The conventional SPECT system usually has two large detectors mounted with parallel-hole collimators. The detectors rotating around the patient provide a sufficient number of untruncated projections. In spite of the advantages offered, the conventional SPECT system is inefficient because only a small portion of the detector area is used to image the heart. In addition, the rotation of the detector during the acquisition produces temporally inconsistent projections and degrades the quality of the image.

In an effort to overcome the limitations of the conventional SPECT system, many groups have proposed dedicated cardiac SPECT systems, *e.g.*, UC San Francisco and Western Cardiology Associate's stationary multipinhole system [1, 2], Discovery NM 530c (GE Healthcare, Haifa, Israel) [3, 4]. A dedicated cardiac SPECT system has the advantage of acquiring consistent projections and ease of performing dynamic studies. In a dedicated cardiac SPECT system, the main drawbacks are data truncation by the small field of view (FOV) and insufficient view-angles.

Image reconstruction from truncated projections falls into two classes: the FOV is 1) partially, or is 2) completely contained by the object; the latter is also known as the interior problem. In 1986, Natterer systematically described this problem and pointed out that the interior problem is not uniquely solvable [5]. Not all tomographic problems with truncated data are interior problems and some may be solvable. For example, in 2004, Noo *et al.* introduced the concept of differentiated backprojection (DBP) so that some truncation problems became solvable for some special truncation geometries [6]. Based on this concept, more recent studies indicate that the solution to the interior problem is unique if the value of a tiny sub-region in the ROI is known [7–10]. Others have investigated this problem from the singular value decomposition (SVD) aspect [11, 12].

To our knowledge, most studies on truncated data tomography presuppose sufficient angular sampling; little has been done for insufficient angular sampling cases [13], as in stationary cardiac SPECT imaging [3, 4, 14]. It has been shown that with sufficient projection views, truncation has a slight bias effect on the reconstruction [15]. However, for many stationary or fast cardiac SPECT systems, view-angles are not sufficient, making the truncation problem more ill-conditioned.

The Maximum-Likelihood Expectation-Maximization (ML-EM) algorithm [16, 17] is the most popular image reconstruction algorithm for nuclear medicine, due to the advantage of

providing accurate modeling of the imaging geometries, physics effects, and Poisson noise. Although the algorithm is robust against noise and systematic inconsistencies when the projection data are not truncated, it may converge to a highly distorted reconstruction if the data are truncated and the view-angles are not sufficient at the same time. To remedy this, we propose a tailored ML-EM algorithm for suppressing the severe streak artifacts and distortion caused by data truncation and insufficient angular sampling. We first tested the reconstruction algorithm on an analytical heart phantom and a pixelated Nurbs-based cardiac-torso (NCAT) phantom [18]. Subsequently, we tested the algorithm on a real Jaszczak torso phantom and its projections were acquired with a SPECT camera using different numbers of view-angles. All of these results indicate that the tailored ML-EM algorithm significantly improve the reconstruction from truncated data using few view-angles, compared to the conventional ML-EM algorithm.

3.3   Theory

3.3.1   Tailored ML-EM Algorithm

The ML-EM algorithm [16, 17], which incorporates physical models of photon emission and detection, is commonly used in emission tomography. Generally, the ML-EM algorithm converges to the maximum likelihood solution after a large number of iterations. In the dedicated cardiac SPECT system, the FOV is usually small and barely covers the heart. As a result, the background and other organs are severely truncated. Another potential drawback of the few-view SPECT system is the lack of a sufficient number of views. Both drawbacks cause part of the object outside the FOV not to be fully scanned by the detector. Therefore, incorrect values (usually extremely large values) appear in pixels outside the FOV, resulting in a highly distorted reconstruction within the FOV. Equation 3.1 displays the conventional ML-EM algorithm [17]

$$x_j^{k+1} = \frac{x_j^k}{\sum_i a_{ij}} \sum_i a_{ij} \frac{p_i}{\sum_m a_{im} x_m^k} \tag{3.1}$$

where p_i is the measured projection, x_j^k is the jth element of the reconstructed image after the kth iteration, and a_{ij} denotes the probability that the photon in pixel j is detected by detector bin i. The summations over i and m present the backprojector and projector, respectively.

In order to suppress the distortion in the reconstruction, we first expand the projection array to match the size of a virtual detector that can measure truncation-free projections. The array expansion does not change the values of measured projection data, but the

unmeasured values are set to the forward-projection of the current estimate of the image. Figure 3.1 illustrates the changes of the coefficient matrix A before and after array expansion. It can be seen that some pixels outside the FOV are not fully covered by all views before expansion. However, the matrix A, whose elements are a_{ij}, is extended and the entire object is fully covered from every view after array expansion.

For a more clear explanation, we write the conventional ML-EM algorithm in an additive form:

$$
\begin{aligned}
x_j^{k+1} &= \frac{x_j^k}{\sum\limits_i a_{ij}} \sum_i a_{ij} \frac{p_i}{\sum\limits_m a_{im} x_m^k} \\
&= \frac{x_j^k}{\sum\limits_i a_{ij}} \sum_i a_{ij} \left(\frac{p_i - \sum\limits_m a_{im} x_m^k}{\sum\limits_m a_{im} x_m^k} + 1 \right) \\
&= x_j^k + \frac{x_j^k}{\sum\limits_i a_{ij}} \sum_i a_{ij} \frac{1}{\sum\limits_m a_{im} x_m^k} \left(p_i - \sum_m a_{im} x_m^k \right).
\end{aligned}
\tag{3.2}
$$

We can see that the adjustment to the ratios $\dfrac{p_i}{\sum\limits_m a_{im} x_m^k}$ does not change the value of $\sum\limits_i a_{ij} \dfrac{1}{\sum\limits_m a_{im} x_m^k} \left(p_i - \sum\limits_m a_{im} x_m^k \right)$, because $\left(p_i - \sum\limits_m a_{im} x_m^k \right)$ is always zero for unmeasured data, before and after array expansion. The array extension only makes the step size $\dfrac{x_j^k}{\sum\limits_i a_{ij}}$ smaller, which decelerates the convergence speed for the pixels outside the FOV. In the conventional ML-EM algorithm, the normal step size $\dfrac{x_j^k}{\sum\limits_i a_{ij}} \approx \dfrac{x_j^k}{nang}$ when there is no truncation, where $nang$ is the number of views. When there is truncation, the step size is approximately $\dfrac{x_j^k}{nang_t}$, where $nang_t$ is the number of views at which the detector can "see" the pixel x_j. In general, $nang_t \leq nang$. Our modified algorithm aims to replace $nang_t$ by $nang$, so that the step size of non-FOV pixels is reduced, and as a result, the reconstruction is better stabilized.

3.4 Experiments

The last section elaborated the reason for using the tailored ML-EM algorithm and provides implementation details. In this section, we design several simulation experiments to verify the advantages of the tailored ML-EM algorithm in the reconstruction of truncated data. The comparisons between the tailored ML-EM algorithm and the conventional ML-EM algorithm are studied using analytical simulation data, Monte Carlo simulation data, and real SPECT data.
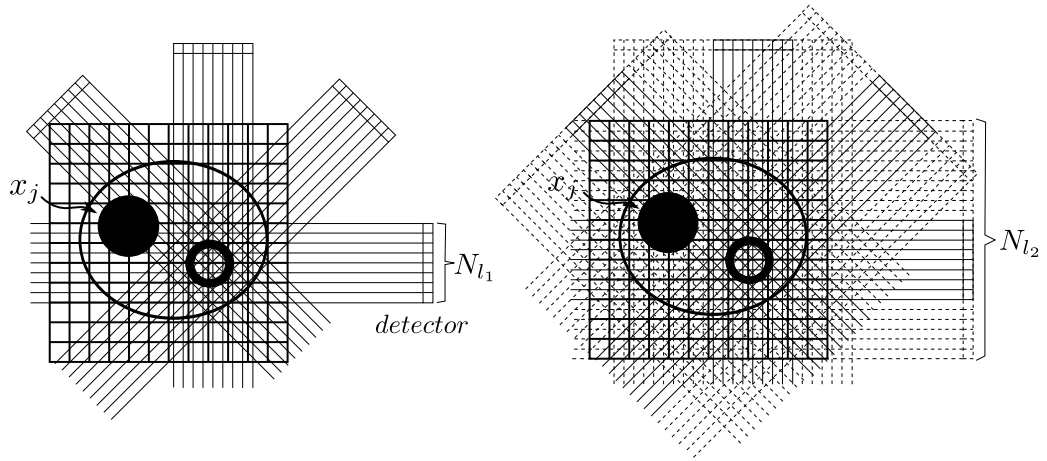
Figure 3.1: The change of $\sum\limits_{i} a_{ij}$ before and after array expansion. The pixel x_j outside the FOV is affected by the array expansion.

3.4.1   Simulated Projections of the Analytical Heart Phantom

A simple 3D heart phantom (Figure 3.2) of size $256\times256\times256$ was used in the first experiment, where the bright hollow sphere represents the left ventricle and the darker sphere and ellipsoid represent other organs/background. Using an analytical projector to generate projections helps to avoid an "inverse crime", which occurs when the same (or very nearly the same) numerical methods are employed in the forward solver and the inversion scheme. In our case, an inverse crime is committed if the reconstruction algorithm uses the same projector that is used to generate the projection data. With the increase in the iteration number, the reconstructed image becomes noisier. For the sake of focusing on the effects of angular sampling and truncation, other effects such as noise, attenuation, collimator blurring, and scattering are not included in this part of the computer simulations. Therefore, the conventional and tailored ML-EM algorithms can iterate to a large number until the reconstructed image converges. In this simulation, the detector size was 64×64, which barely contained the heart. Both the conventional ML-EM algorithm and the tailored ML-EM algorithm were stopped at the 500th iteration where the reconstructed image almost converged.

3.4.2   Simulated Projections of the NCAT Phantom

In the second set of computer simulations, a 3D numerical myocardial phantom (NCAT phantom) [18] and the GATE (Geant4 Application for Tomographic Emission) Monte Carlo simulation tool [19, 20] were used to generate more realistic projections, which include the effects of noise, attenuation, collimator-detector response, and scatter. The Monte Carlo code simulated a dual-head SPECT system, which has a FOV of 53.3×38.7 cm and a low-energy high-sensitivity (LEHS) collimator (hole length 24.05 mm and diameter 1.11 mm), and acquired 60 or 14 projections over a range of 180°. The projection data were acquired in 64×64 arrays with a pixel size of 6.25 mm. The distance between the detector and the axis of rotation was 29 cm. For isotope ^{99m}Tc, a photopeak window of 140 keV $\pm$ 10% was used in the simulation. Small FOV (12×12 cm) projections were obtained from full FOV projections by removing the pixels outside the small FOV. Due to noise, only 10 iterations were used in the reconstruction algorithms.

3.4.3   Real Emission Data Using Jaszczak Torso Phantom

A realistic emission data set was acquired using a Siemens E-CAM Signature Series® SPECT scanner with low-energy high-resolution collimators (hole length 24.05 mm, hole diameter 2.54 mm) (Figure 3.3b). The thorax phantom used in this experiment was the

(a) The 110th slice (b) The 120th slice (c) The 128th slice
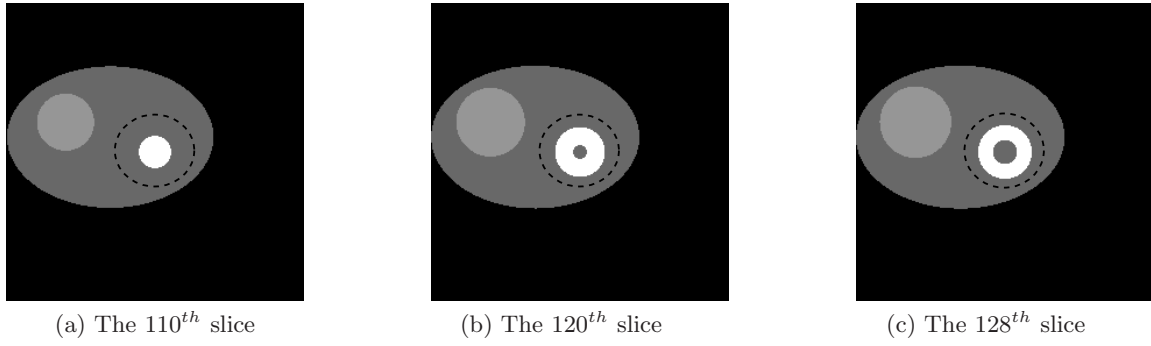
Figure 3.2: From left to right: the 110th, 120th, and 128th axial slices of the 3D heart phantom. The FOV covered by the small detector is indicated by the dashed circle.

(a) (b)

Figure 3.3: Jaszczak torso phantom and SPECT scanner. (a) The Jaszczak torso phantom. (b) The Siemens E-CAM Signature Series$^{®}$ SPECT scanner used in the experiment.

large Jaszczak torso phantom consisting of the lungs, liver, bones, and cardiac insert, as shown in Figure 3.3a. A circular orbit with a radius of 26.7 cm was used. In order to reduce the acquisition time, the activities in all organs as well as in the background were increased 6 times; during data acquisition we used 1/6 of the normal acquisition time. A total activity of 1480 MBq (40,000 μCi) ^{99m}Tc was injected into various parts of the phantom, with 740 MBq (20,000 μCi; $\sim$16μCi/cc) in the liver, 148 MBq (4,000 μCi; $\sim$37μCi/cc) in the cardiac wall , and 592 MBq (16,000 μCi; $\sim$1.8μCi/cc) in the major chamber. Therefore, the acquisition time was reduced to about 1/6 that of the ASNC protocol [21] for a low count rest study. Projection sets with view-angles of 60, 20, and 10 were acquired, respectively. The acquisition time varied with the projection number to keep the total counts approximately the same. The size of the projection array was 256×256. A small data set (58×58) was cut out from the full FOV to generate the truncated data.

3.4.4   Assessment of Image Quality

Different methods were used to evaluate the quality of the conventional ML-EM and the tailored ML-EM reconstruction. For the noise-free images in the analytical heart phantom study, we measured the average activity in the myocardium as l and the average activity in a surrounding region within the FOV as b. The contrast was then defined by

$$Contrast = \frac{|l - b|}{l + b}. \tag{3.3}$$

The ratio of reconstruction contrast and phantom contrast was defined as relative contrast. The mean squared error (MSE) with N voxels in the FOV was calculated as follows:

$$MSE = \frac{1}{N} \sum_{i=1}^{N} (x_i - x_i^{true})^2. \tag{3.4}$$

For further quantitative assessment, image profiles through a central slice of the reconstructed images are shown and compared in all three experiments.

3.5   Results

In this section, we compared the reconstruction results of the conventional ML-EM algorithm and the tailored ML-EM. For display purposes only, all images were scaled to [0 255] and were displayed using the same linear gray scale.

3.5.1   Simulated Projections of the Analytical Heart Phantom

The simulation results obtained from the reconstruction of the analytical heart phantom, together with corresponding vertical profiles through the center of the heart, are shown

in Figures 3.4 and 3.5 for the conventional ML-EM algorithm and the tailored ML-EM algorithm, respectively.

Figure 3.4 shows the 120th and 128th slices from the 3D reconstruction results as representatives. At 60 view-angles, the results from the conventional ML-EM algorithm are similar to those from the tailored ML-EM algorithm, except for the presence of a dark line in the center of the ventricular wall, which degrades the uniformity of the myocardium. Streak artifacts are observed outside the truncation edge of the conventional ML-EM reconstructed image. The profiles in Figure 3.5a show a large bias between the profile of the conventional ML-EM reconstructed image and that from the phantom. However, the profile curve of the tailored ML-EM reconstructed image follows that of the phantom reasonably well. At 20 and 10 views, the reconstruction results of the conventional ML-EM algorithm show greater distortion, especially at 10 view angles. In other words, the distortion increases as the number of view angles decreases from 60 to 10. The profiles in Figures 3.5b and 3.5c show
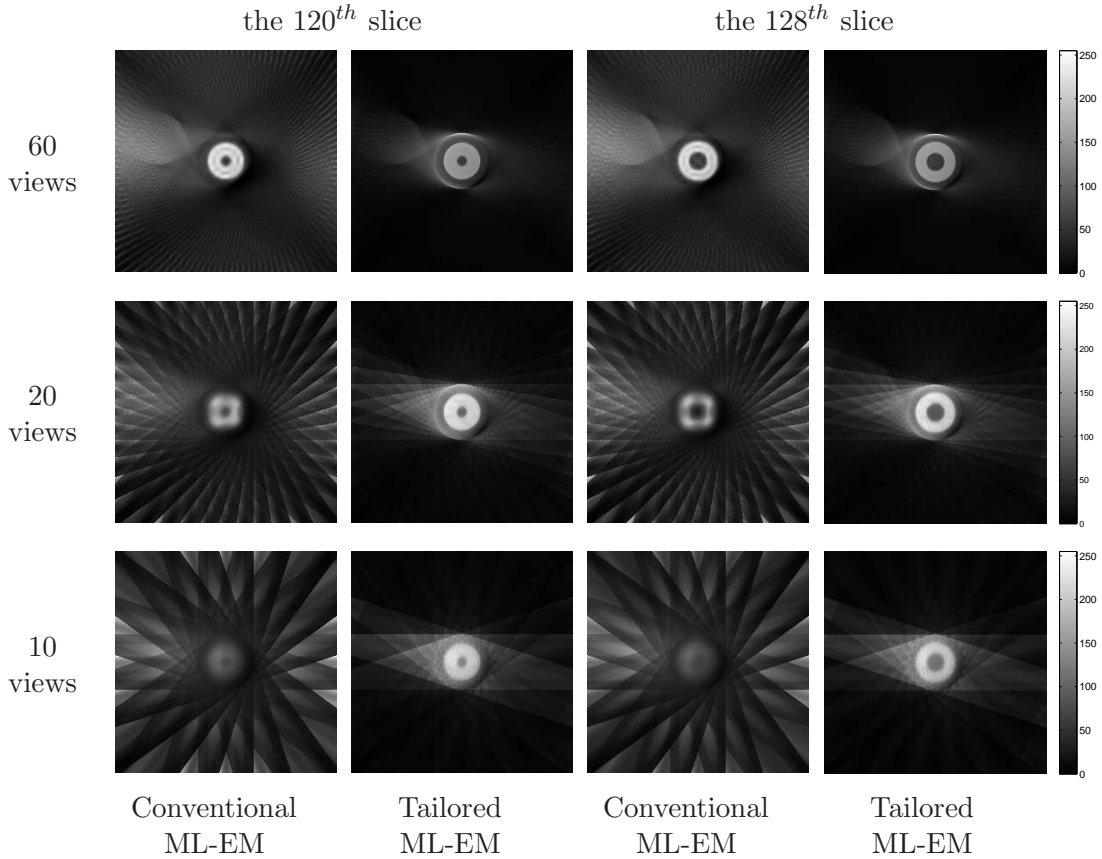
Figure 3.4: Images of the analytical heart phantom reconstructed by the conventional ML-EM and the tailored ML-EM algorithms using different number of views. The projections were truncated and 500 iterations were applied.
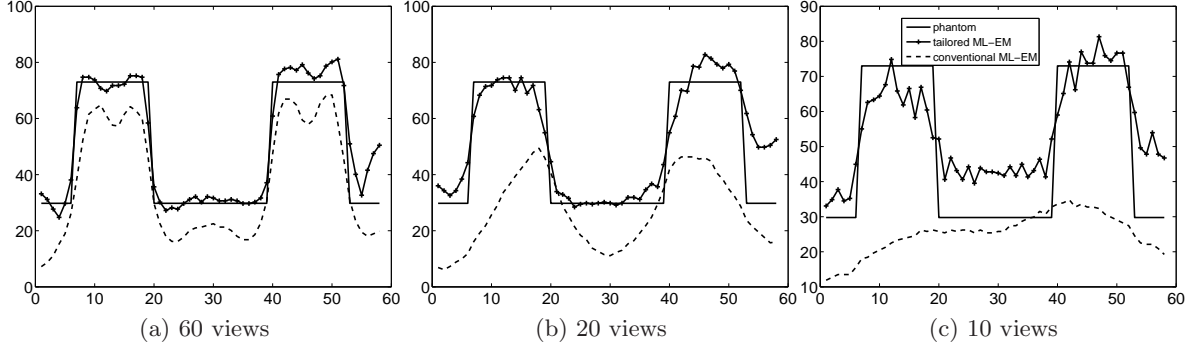
Figure 3.5: The vertical profiles through the center of slice 128 of the analytical heart phantom and the reconstructed images using the conventional ML-EM and the tailored ML-EM algorithms. The images were reconstructed from 60, 20, and 10 truncated projections. The solid line represents the true heart phantom, the solid line with plus sign represents the tailored ML-EM reconstruction, and the dash line represents the conventional ML-EM reconstruction.

large biases between the conventional ML-EM results and the phantom. Competitively, the tailored ML-EM algorithm has fairly good image quality at 20 views as well as at 10 views.

The relationship between the MSE and the relative contrast for the conventional ML-EM and the tailored ML-EM reconstruction is shown in Figure 3.6. The tailored ML-EM has a much lower MSE than the conventional ML-EM at the same relative contrast level, indicating a more accurate reconstruction. The relative contrast of the conventional ML-EM reconstruction is larger than 1 at the number of views higher than 10, due to a large number of voxels in the background close to the edge of FOV that are nearly equal to zero. This can also be seen in Figure 3.5. In this situation, the value of voxels in the background is incorrect. Therefore, a large MSE is observed for the conventional ML-EM reconstruction. With the reduction of the number of view-angles, the MSE increases and the relative contrast decreases. At 10 view-angles, the tailored ML-EM reconstruction has higher relative contrast and a lower MSE than the conventional ML-EM reconstruction.

We also compared the two algorithms at different iterations, as shown in Figure 3.7. The reconstructed image from truncated projections using the conventional ML-EM algorithm starts to deteriorate once the iteration number is larger than 5. Furthermore, it converges to a nonuniform shape after 10 iterations. High-frequency artifacts occur outside the FOV; as a consequence, they propagate into the FOV. The tailored ML-EM algorithm significantly suppresses the artifacts and improves the image quality in all cases.
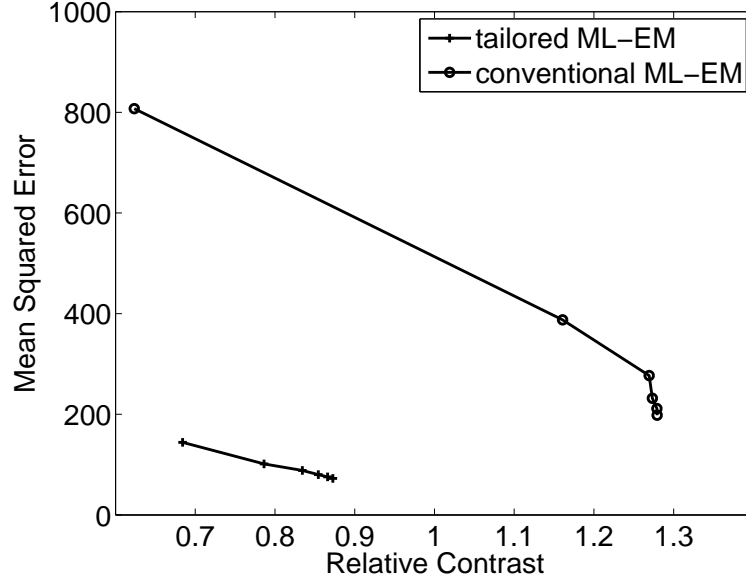
Figure 3.6: MSE as a function of relative contrast in the reconstructed analytical heart phantom using conventional ML-EM and tailored ML-EM algorithms. The points on the curves represent the numbers of views. For each curve, the view number increases from the left side to the right side.
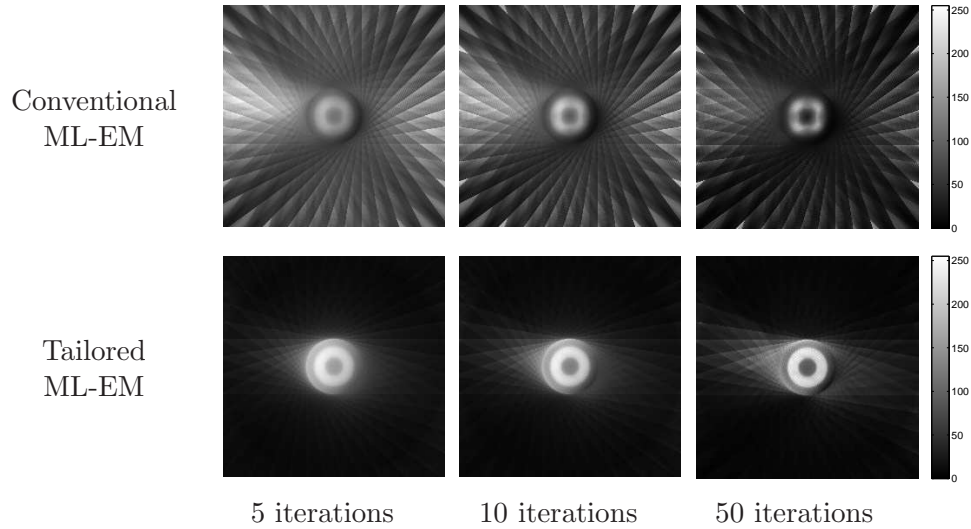
Figure 3.7: Sample reconstructed central axial slices of the conventional ML-EM and the tailored ML-EM reconstructions at different iterations in the analytical heart phantom experiment. All images were reconstructed from 20 truncated projections.

3.5.2   Simulated Projections of the NCAT Phantom

We next used more realistic Monte Carlo data, including attenuation, scatter, noise, and distance-dependent collimator resolution, to compare the conventional ML-EM algorithm and the tailored ML-EM algorithm. Similar observations are made at 60 truncated projections and no distortion is evident. The conventional ML-EM results at 14 view-angles shows lower quality, where more severe streak artifacts outside the truncation edge and lower contrast are obtained as compared to those from the tailored ML-EM algorithm (see Figure 3.8).

The profiles in Figure 3.9 show only small differences between the conventional and tailored ML-EM reconstructions at 60 views. Nevertheless, the profiles of the conventional ML-EM reconstruction have much lower counts at 14 views.
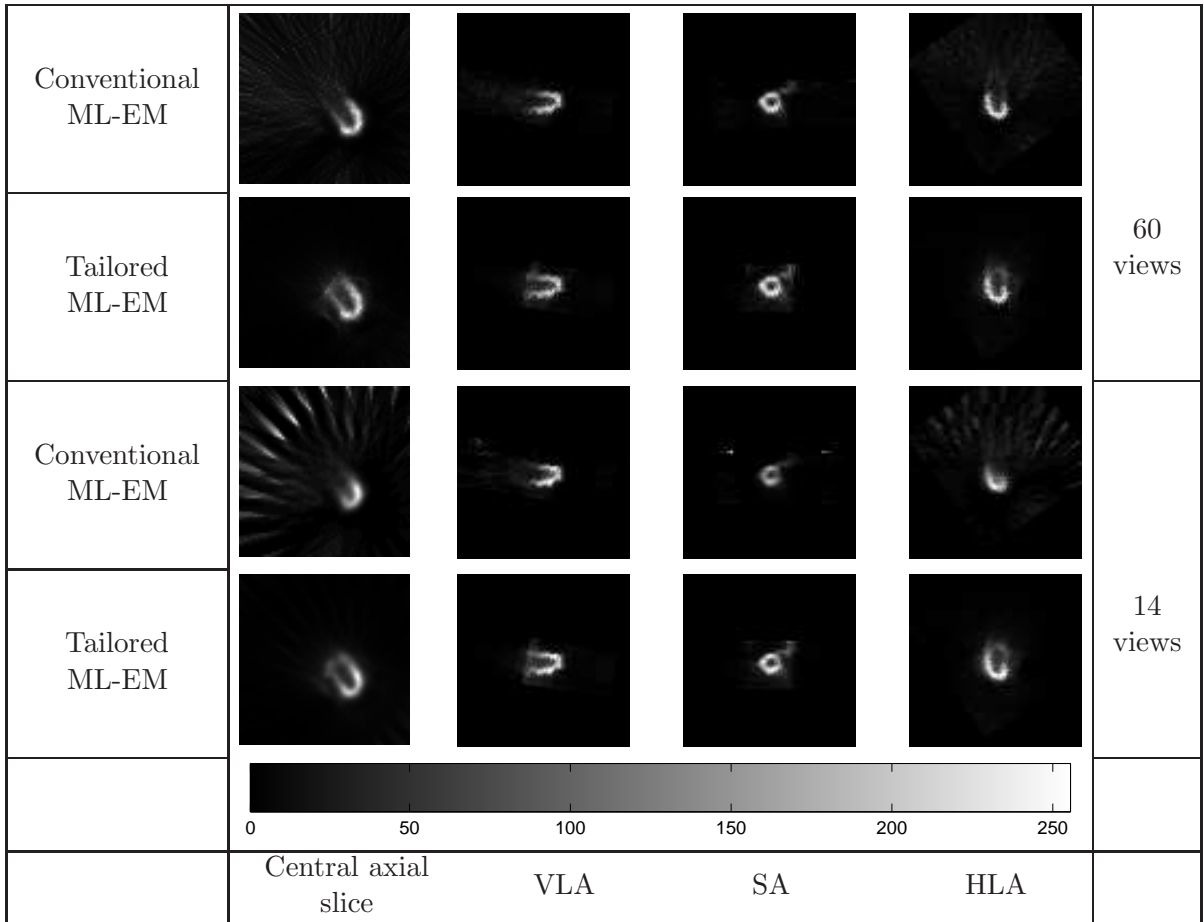
Figure 3.8:   The reconstruction results of Monte Carlo simulation using the NCAT phantom. The first column shows the central slices of the reconstructions. Vertical long-axis (VLA), short-axis (SA), and horizontal long-axis (HLA) cuts are shown in the last three columns. 10 iterations were used.
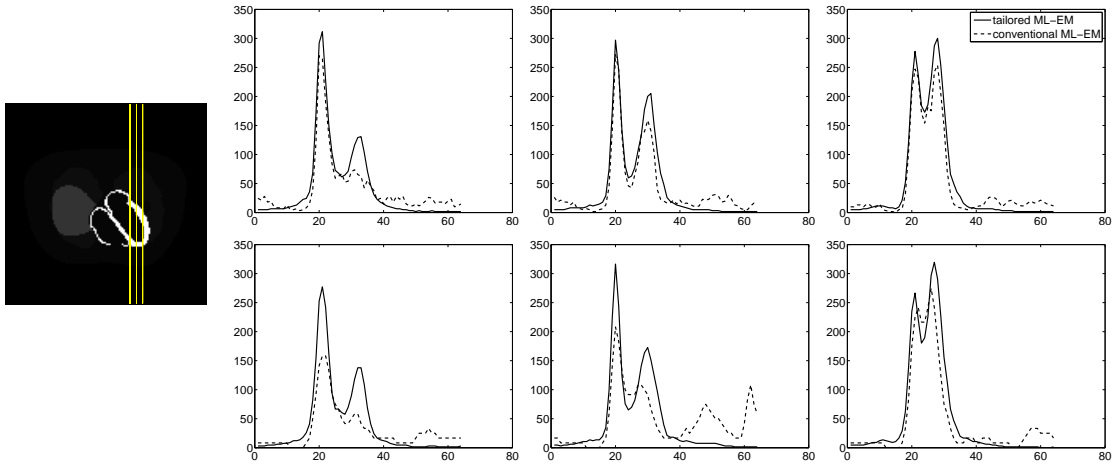
Figure 3.9: The vertical profile curves for slice 128 of reconstructed images with 60 (top row) and 14 views (bottom row). Solid lines on slice 128 of the NCAT phantom indicate the profile positions. The profiles on the right side correspond to the lines from left to right in the left-hand image.

These results reconfirm that the tailored ML-EM algorithm is superior to the conventional ML-EM algorithm for reconstruction of acquisitions with small numbers of views and truncated data. The Monte Carlo simulations provide a better impression of the advantages of the tailored ML-EM algorithm. No attenuation, scatter, and blurring corrections are performed during image reconstruction in this paper.

3.5.3   Real Emission Data Using Jaszczak Torso Phantom

Given the highly encouraging results with the noise-free analytical heart phantom and the noisy NCAT phantom, we next proceeded to real emission SPECT data using a Jaszczak torso phantom. Each reconstruction was stopped at the $30th$ iteration. Overall the image quality is better for the results of the tailored ML-EM algorithm than those of the conventional ML-EM algorithm (Figure 3.10 and 3.11). Moreover, the tailored ML-EM algorithm decelerates the convergence speed and keeps the value of pixels outside the FOV under control. When the number of view-angles is small, superior myocardial edge definition in the images obtained by using the tailored ML-EM algorithm is again evident (see Figure 3.11).

Figure 3.10 clearly shows the advantages of the tailored ML-EM algorithm at the reconstruction of truncated projection data at small number of view-angles. The shape of the heart is well conserved even when the number of view-angles is less than 20.
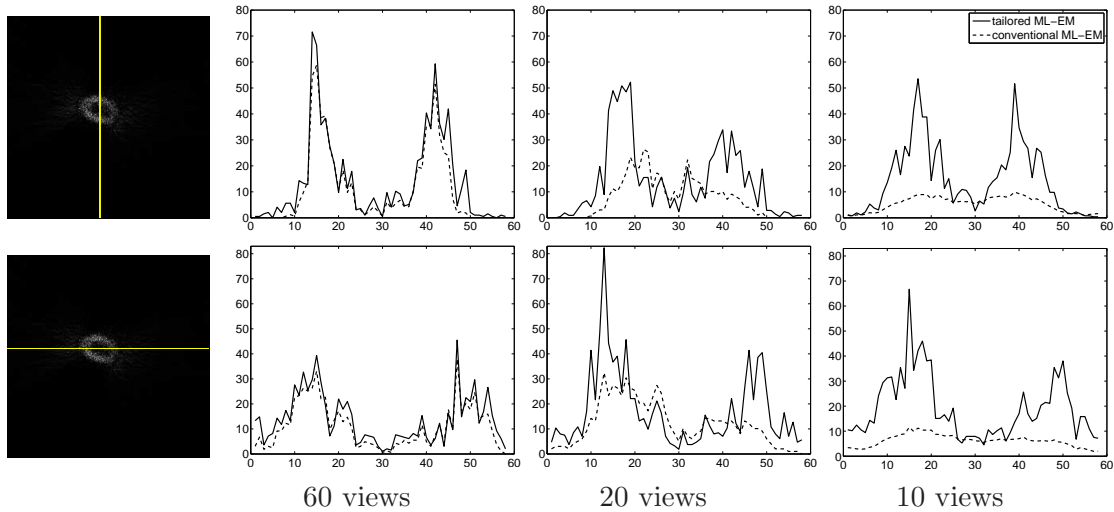
Figure 3.10: The vertical profiles for slice 128 of the reconstructed images using conventional ML-EM and tailored ML-EM algorithms. The images were reconstructed from 60, 20, and 10 truncated projections. Solid lines on slice 128 of the reconstructed images indicate the profile positions.

	Central axial slice	VLA	SA	HLA	
Conventional ML-EM					60 views
Tailored ML-EM					
Conventional ML-EM					20 views
Tailored ML-EM					
Conventional ML-EM					10 views
Tailored ML-EM					

Figure 3.11: The reconstruction results obtained from physical phantom study. From top to bottom: the reconstruction results of 60, 20, and 10 truncated projections, respectively. The first column shows the central slices of the reconstructions. Vertical long-axis (VLA), short-axis (SA), and horizontal long-axis (HLA) cuts are shown in the last three columns. 30 iterations were used.

3.6   Discussion and Conclusions

A tailored ML-EM algorithm has been proposed for the reconstruction of projection data with insufficient angular sampling and data truncation. Under these conditions, the analytical heart phantom, NCAT phantom, and Jaszczak torso phantom simulation results verify that the tailored ML-EM algorithm provides a clear improvement in reconstructed image quality and accuracy, compared with the conventional ML-EM algorithm. The tailored algorithm chooses a smaller step size for pixels outside the FOV to stabilize the iterative algorithm, which in turn suppresses the streak artifacts outside the FOV and reduces distortion in the FOV.

For a sufficient number of views, such as 60 view-angles, the effect of truncation on the reconstruction is negligible and no significant difference is observed between the reconstruction results of the tailored ML-EM algorithm and those of the conventional ML-EM algorithm.

Truncation mainly affects the reconstruction at small numbers of projections, where the conventional ML-EM algorithm performs poorly. Insufficient angular sampling makes the truncation artifacts more severe. As a result, severe artifacts appear outside the FOV. The errors outside the FOV propagate into the FOV as the iteration number increases, causing distortion in the reconstruction of the conventional ML-EM algorithm. In addition, the presence of bias in the background increases the MSE and reduces the relative contrast of images. Nonetheless, the streak artifacts and image distortion are significantly reduced after using the tailored ML-EM algorithm. The shape and the value of the heart are well conserved at 10 view-angles, even when data truncation is present.

In conclusion, the tailored ML-EM algorithm can substantially suppress the artifacts and distortions associated with small FOV cardiac imaging. It also extends the conventional ML-EM algorithm to the reconstruction of truncated projections at small number of views. The data extension strategy in the tailored ML-EM algorithm can be directly extended into the OS-EM algorithm.

3.7   Acknowledgments

3.8   References

[1] T. Funk, D. Kirch, J. Koss, E. Botvinick, and B. Hasegawa, "A novel approach to multipinhole SPECT for myocardial perfusion imaging," *J. Nucl. Med.*, vol. 47, no. 4,

pp. 595–602, 2006.

[2] P. Steele, D. Kirch, and J. Koss, "Comparison of simultaneous dual-isotope multip-inhole SPECT with rotational SPECT in a group of patients with coronary artery disease," *J. Nucl. Med.*, vol. 49, no. 7, pp. 1080–1089, 2008.

[3] F. Esteves, P. Raggi, R. Folks, Z. Keidar, J. Wells Askew, S. Rispler, M. OConnor, L. Verdes, and E. Garcia, "Novel solid-state-detector dedicated cardiac camera for fast myocardial perfusion imaging: multicenter comparison with standard dual detector cameras," *J. Nucl. Cardiol.*, vol. 16, no. 6, pp. 927–934, 2009.

[4] M. Bocher, I. Blevis, L. Tsukerman, Y. Shrem, G. Kovalski, and L. Volokh, "A fast cardiac gamma camera with dynamic SPECT capabilities: design, system validation and future potential," *Eur. J. Nucl. Med. Mol. Imag.*, vol. 37, no. 10, pp. 1887–1902, 2010.

[5] F. Natterer, *The mathematics of computerized tomography*, vol. 32. Society for Industrial Mathematics, 2001.

[6] F. Noo, R. Clackdoyle, and J. Pack, "A two-step Hilbert transform method for 2D image reconstruction," *Phys. Med. Biol.*, vol. 49, p. 3903, 2004.

[7] M. Defrise, F. Noo, R. Clackdoyle, and H. Kudo, "Truncated Hilbert transform and image reconstruction from limited tomographic data," *Inverse Problems*, vol. 22, p. 1037, 2006.

[8] Y. Ye, H. Yu, Y. Wei, and G. Wang, "A general local reconstruction approach based on a truncated Hilbert transform," *J. Biomed. Imaging*, vol. 2007, p. 63634, 2007.

[9] H. Kudo, M. Courdurier, F. Noo, and M. Defrise, "Tiny a priori knowledge solves the interior problem in computed tomography," *Phys. Med. Biol.*, vol. 53, p. 2207, 2008.

[10] H. Yu and G. Wang, "Compressed sensing based interior tomography," *Phys. Med. Biol.*, vol. 54, p. 2791, 2009.

[11] P. Maass, "The interior Radon transform," *SIAM J. Appl. Math.*, pp. 710–724, 1992.

[12] G. Zeng and G. Gullberg, "An SVD study of truncated transmission data in SPECT," *IEEE Trans. Nucl. Sci*, vol. 44, no. 1, pp. 107–111, 1997.

[13] G. Zeng and G. Gullberg, "Null-space function estimation for the interior problem," *Phys. Med. Biol.*, vol. 57, p. 1873, 2012.

[14] E. Garcia and T. Faber, "New trends in camera and software technology in nuclear cardiology," *Cardiol. Clin.*, vol. 27, no. 2, pp. 227–236, 2009.

[15] J. Xiao, F. Verzijlbergen, M. Viergever, and F. Beekman, "Small field-of-view dedicated cardiac SPECT systems: impact of projection truncation," *Eur. J. Nucl. Med. Mol. Imag.*, vol. 37, no. 3, pp. 528–536, 2010.

[16] L. Shepp and Y. Vardi, "Maximum likelihood reconstruction for emission tomography," *IEEE Trans. Med. Imaging*, vol. 1, no. 2, pp. 113–122, 1982.

[17] K. Lange, R. Carson, *et al.*, "EM reconstruction algorithms for emission and transmission tomography," *J. Comput. Assist. Tomogr.*, vol. 8, no. 2, pp. 306–316, 1984.

[18] W. P. Segars, *Development of a new dynamic NURBS-based cardiac torso (NCAT) phantom.* PhD thesis, University of North Carolina, 2001.

[19] D. Strulab, G. Santin, D. Lazaro, V. Breton, and C. Morel, "GATE (Geant4 Application for Tomographic Emission): a PET/SPECT general-purpose simulation platform," *Nucl. Phys. B (Proc. Suppl.)*, vol. 125, pp. 75–79, 2003.

[20] S. Jan, G. Santin, D. Strul, S. Staelens, K. Assie, D. Autret, S. Avner, R. Barbier, M. Bardies, P. Bloomfield, *et al.*, "GATE: a simulation toolkit for PET and SPECT," *Phys. Med. Biol*, vol. 49, no. 19, p. 4543, 2004.

[21] "American society of nuclear cardiology - guidelines and standards." [Online]. Available from: `http://www.asnc.org/`. [Accessed 9th April 2013].

CHAPTER 4

SPECIAL WEIGHTING FOR ZERO-VALUED PROJECTIONS IN THE ML-EM ALGORITHM

4.1 Abstract

The maximum-likelihood expectation-maximization (ML-EM) algorithm is the most popular image reconstruction algorithm for nuclear medicine. We found that zero values in the projection data need special attention in an image reconstruction algorithm. In this paper, we propose a method that introduces a positive constant weighting factor c to zero-valued projections in the ML-EM algorithm. By modifying the c value, the weighting for the projections whose values are equal to zero is changed, which in turn affects the reconstruction of the object. Computer simulations confirm that applying an appropriate weighting for zero-valued projections can result in fewer image errors than the conventional ML-EM algorithm. The comparison studies are presented between the ML-EM algorithm with a special weighting for zero-valued projections (zML-EM) and the conventional ML-EM algorithm.

4.2 Introduction

The maximum-likelihood expectation-maximization (ML-EM) algorithm [1] has a sturdy theoretical basis and is being widely used in emission image reconstruction. The ML-EM algorithm has the advantage of providing accurate modeling of the imaging geometries, physics effects, and Poisson noise [2–4].

The ML-EM algorithm is often applied to single photon emission tomography (SPECT) and positron emission tomography (PET) emission data reconstruction. Recently, high-speed acquisition and dynamic studies are usually performed in cardiac or brain imaging, generating low count data. However, in low count imaging, all image reconstruction algorithms perform poorly. When the measured count is very low, there is a probability that a zero-valued projection is measured, while its true value is a positive value. This can

also happen when a preprocessing method is applied to correct for scattering. When the iterative algorithm is close to convergence, the line-integral of the image associated with the wrong zero-valued projection will converge to zero and drive all image pixels along this particular line to zero. In addition, the ML-EM algorithm tends to generate noise in the image unless stopped early. Such early termination is necessary for low count data which have a relatively high noise level, but early termination tends to cause loss of the sharpness of edges, especially the boundary.

A zero-valued projection is not always wrong. A zero-valued projection is correct when measuring the area outside the object, even though there is scattering. This paper considers some special treatments for zero measurements. Unlike positive measurement values, when the projection measurement is zero, one is certain that the measurement is correct if the projection ray does not pass through the radiation source body and one is certain that the measurement is wrong if the projection ray passes through the body. In this paper, we introduce a positive weighting factor c to the ML-EM algorithm. By adjusting the weighting factor c for different kinds of zero values in the projection data, the reconstructed image shows smaller errors than that of the conventional ML-EM algorithm.

This paper is organized as follows. In Section 4.3, we review the formulation of the conventional ML-EM algorithm and the new method of changing the weighting of zero-valued projections in the ML-EM algorithm (zML-EM). Section 4.3.3 briefly discusses the noise property of the zML-EM algorithm. A count conservation property is presented in Section 4.3.4. In Section 4.4, we use the two different algorithms to reconstruct low count data and the results are compared by calculating the image error in the region of interest (ROI).

4.3   Theory

4.3.1   The Conventional ML-EM Algorithm (ML-EM)

The conventional ML-EM algorithm proposed by Shepp and Vardi [1] and Lange and Carson [5] can be expressed as

$$x_j^{k+1} = \frac{x_j^k}{\sum\limits_i a_{ij}} \sum\limits_i a_{ij} \frac{p_i}{\sum\limits_m a_{im} x_m^k} \tag{4.1}$$

where p_i is the measured projection and a_{ij} is the probability that the photon in pixel j is detected by detector bin i. The summations over i and m denote the back-projector and projector, respectively. The ratio of the actual measurement p_i to the estimated

measurement $\sum\limits_{m} a_{im} x_m^k$ is back-projected to the image domain. Then the ratio of two back-projections is used to update the image x_j^k after the kth iteration.

The above ML-EM algorithm can also be rewritten in the gradient descent form as

$$X^{k+1} = X^k + S^k A^T \Lambda^k (P - AX^k), \tag{4.2}$$

where

$$S^k = \text{diag}\left\{ \frac{x_j^k}{\sum\limits_i a_{ij}} \right\} \tag{4.3}$$

represents the step size and

$$\Lambda^k = \text{diag}\left\{ \frac{1}{\sum\limits_m a_{im} x_m^k} \right\} \approx \text{diag}\left\{ \frac{1}{\bar{p}_i} \right\} \tag{4.4}$$

is the projection data weighting which is the reciprocal of the noise variance matrices. The components of matrices A, X, and P are a_{ij}, x_j, and p_i, respectively.

4.3.2 Weighting of Zero-Valued Projections in the ML-EM Algorithm (zML-EM)

The ML-EM algorithm is a powerful tool in emission image reconstruction for properly modelling the Poisson statistics in the measurements. All algorithms (including the ML-EM algorithm) perform poorly in low count imaging, for example, in gated imaging. We would like to improve the performance of the ML-EM algorithm in low count imaging. A low count projection measured in each projection bin implies a relatively low signal-to-noise ratio (SNR). There is thus a probability that zero values occur inside the projection data due to noise or a subtraction operation, leading to black streak artifacts in the reconstructed image. In practice, the ML-EM algorithm is terminated early to reduce noise in the reconstruction, but this also causes blurred edges in the image.

To remedy this, we introduce a positive weighting factor c_i to the ML-EM algorithm for the zero-valued projection data. Therefore, the projection weighting as stated in Equation 4.4 is changed to

$$\Lambda^k = \text{diag}\left\{ \frac{c_i}{\sum\limits_m a_{im} x_m^k} \right\}. \tag{4.5}$$

The value of c_i is normally set to ONE for projection measurements which are positive.

Case 1: If we believe a zero measurement is correct (*e.g.*, it is outside the radiation body), we would further emphasize this measurement by setting $c_i > 1$.

Case 2: If we believe a zero measurement is incorrect (*e.g.*, its neighboring values are non-zero), we would de-emphasize this measurement by setting $0 \leq c_i < 1$.

By modifying the ML-EM algorithm with the newly introduced weighting factor c_i, the zML-EM algorithm is obtained and given by

$$x_j^{k+1} = \frac{x_j^k}{\sum_i a_{ij} c_i} \sum_i a_{ij} c_i \frac{p_i}{\sum_m a_{im} x_m^k}, \tag{4.6}$$

where the c_i value is defined as

$$c_i = \begin{cases} 1, & p_i \neq 0 \\ 0 \leq \text{const} < 1, & p_i = 0 \quad \text{outside the object region} \\ \text{const} > 1, & p_i = 0 \quad \text{inside the object region} \end{cases} \tag{4.7}$$

Case 1 is better illustrated when the iteration number is low, while Case 2 is better illustrated when the iteration number is very high.

4.3.3   Noise Property of zML-EM

The zML-EM algorithm preserves most properties of the ML-EM algorithm, such as the noise property derived in Barrett's paper [6]. The variance expression of the image at each iteration of the zML-EM is almost identical to that of the ML-EM in [6], except that the back-projection of constant 1 (*i.e.*, the summation $\sum_i a_{ij}$) is replaced by the back-projection of function c_i (*i.e.*, the summation $\sum_i a_{ij} c_i$). Similar to Barrett's conclusion, the variance and covariance of noise in the zML-EM reconstruction can be calculated as a function of the object, system matrix, and iteration number [6]. When the number of iterations gets larger, the image system will suffer from more noise amplification. The results of computer simulations show that the zML-EM requires fewer iterations than the ML-EM to reach the minimum image error.

4.3.4   Count Conservation Property of zML-EM

The zML-EM algorithm also retains ML-EM's count conservation property that the weighted sum of the forward projections at each iteration is the same as the total number of counts in the original projection data. In fact,

$$\sum_i c_i \sum_j a_{ij} x_j^{k+1} = \sum_i c_i \sum_j a_{ij} \cdot \left(\frac{x_j^k}{\sum_n a_{nj} c_n} \sum_n a_{nj} c_n \frac{p_n}{\sum_m a_{nm} x_m^k} \right). \tag{4.8}$$

Changing the order of the two outermost summations yields

$$\sum_i c_i \sum_j a_{ij} x_j^{k+1} = \sum_j x_j^k \frac{\sum_i a_{ij} c_i}{\sum_n a_{nj} c_n} \sum_n a_{nj} c_n \frac{p_n}{\sum_m a_{nm} x_m^k}. \tag{4.9}$$

We notice that two summations $\sum_i a_{ij}c_i$ and $\sum_n a_{nj}c_n$ can be cancelled. Then changing the order of summation again, we get that

$$\sum_i c_i \sum_j a_{ij}x_j^{k+1} = \sum_n p_n c_n \frac{\sum_j a_{nj}x_j^k}{\sum_m a_{nm}x_m^k} = \sum_n p_n c_n = \sum_n p_n. \tag{4.10}$$

The last equation in (4.10) holds because $c_n = 1$ when $p_n \neq 0$.

4.4   Computer Simulations

A heart phantom of size 128×128 was used in the computer simulations, as shown in Figure 4.1a. In case 1, for the zero-valued projection outside the object (as seen in Figure 4.1b case 1), a c value greater than 1 was used in the zML-EM algorithm. In order to maintain the noise at a low level while preserving the signal in the reconstructed images, the algorithm was stopped after a small number of iterations. In case 2, two projections inside the object region were randomly selected and set to zero for the purpose of simulating zero values inside the object region due to the effect of noise. Both ML-EM and zML-EM algorithms were terminated at 30 iterations for a better observation of streak artifacts. Poisson noise was added to all projections.

The simulation results were evaluated by comparing the image error in the region of interest (ROI), which was calculated as follows:

$$Image\ error = \frac{1}{N} \sum_{i=1}^{N} \left| x_i - x_i^{true} \right|. \tag{4.11}$$

(a)   (b)
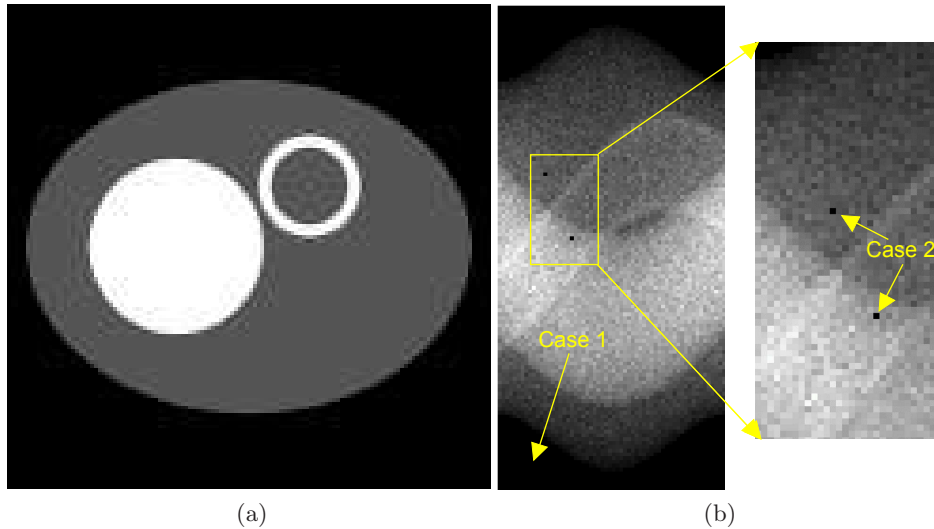
Figure 4.1: Heart phantom and zeros values in its projection. (a) The heart phantom. (b) The zero values in the projection.

For further quantitative assessment, visual inspection of object shape and image arti-facts, and image profiles through the reconstructed images are shown and compared.

4.5 Results

4.5.1 Simulation Results of Case 1

Figure 4.2 shows the reconstruction results of ML-EM and zML-EM algorithms in case 1. Both algorithms were stopped at 6 iterations before the images became noisier. As seen in the upper left of Figure 4.2, the image reconstructed by the ML-EM algorithm has a blurred boundary, which spreads into the background, causing inaccurate values in these pixels. By comparison, after applying a c value that is greater than 1, the pixels in the background converge to the actual value–zero quickly. Correspondingly, the boundary of the heart phantom was accurately reconstructed by using the zML-EM algorithm. When the number of iterations increases to 80, the image reconstructed by the ML-EM algorithm is similar to that from the zML-EM algorithm. Both algorithms converge to zero at the background. At the same time, much noise was observed in the reconstructed images. Although scattering occurs in reality, most of the pixels at the background are zeros at low count images.

The image error between the reconstruction and the phantom is plotted as a function of the iteration number. As shown in Figure 4.3, the image error first decreases and then increases with the iteration number. For a small number of iterations, where the image error decreases, the zML-EM reconstructed image always has fewer errors than that of the ML-EM, which means that the image reconstructed by the zML-EM algorithm is more accurate. At a higher number of iterations, the zML-EM reconstructed image has a similar image error to that from the ML-EM algorithm.

The profiles through the reconstructions of the ML-EM and zML-EM algorithms at 6 iterations are plotted in Figure 4.4. Compared with the ML-EM result, the profile curve of the zML-EM reconstructed image follows that of the phantom well near the boundary. Bigger differences are seen between the profiles of the ML-EM result and the phantom.

4.5.2 Simulation Results of Case 2

The simulation results of case 2 are displayed in Figure 4.5. Without any correction, the ML-EM result shows two black lines in the image due to the zero-values inside the object region data. With a change of the c value to a very small number that is less than 1 (such as 0.000001), the two black lines were removed in the reconstruction result of the zML-EM algorithm.
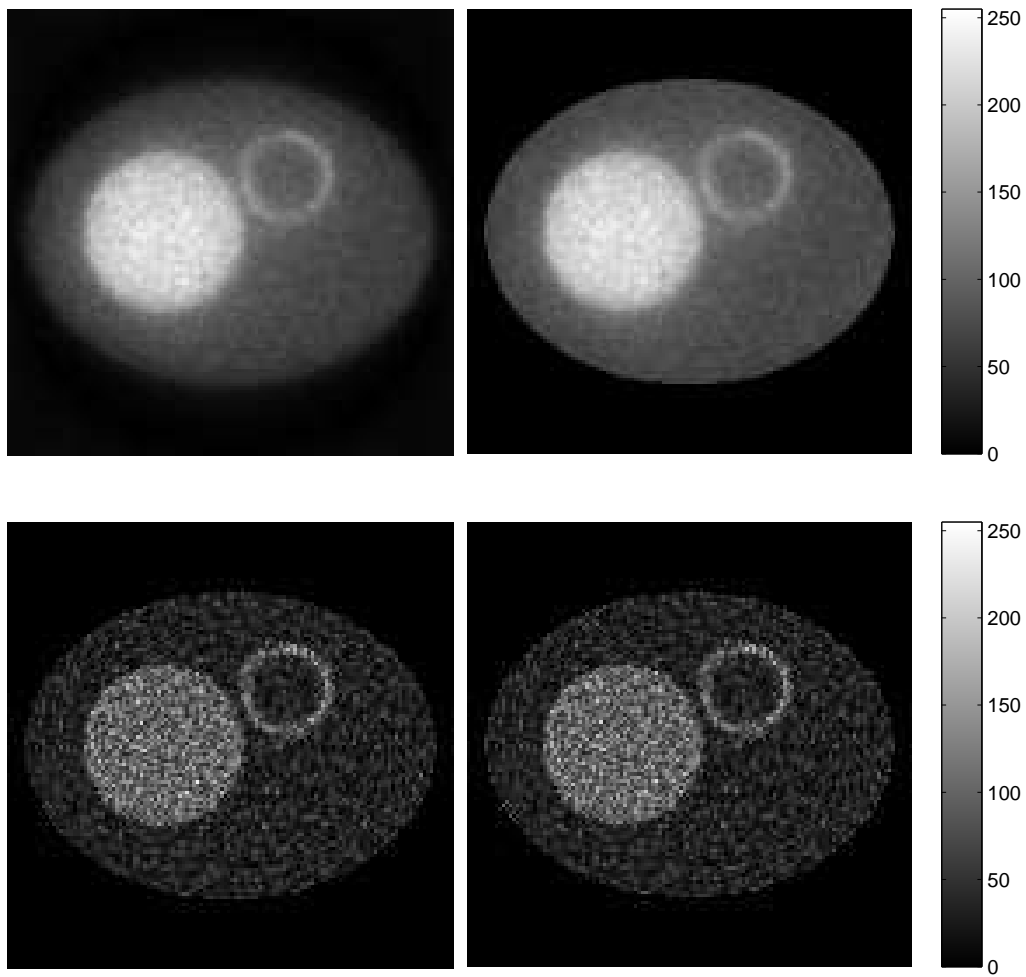
Figure 4.2: The reconstruction results of 60 views using ML-EM (left) and zML-EM (right) algorithms, respectively. In the zML-EM algorithm, $c=8$ was applied for the zero-valued projections. Top row: 6 iterations. Bottom row: 80 iterations.
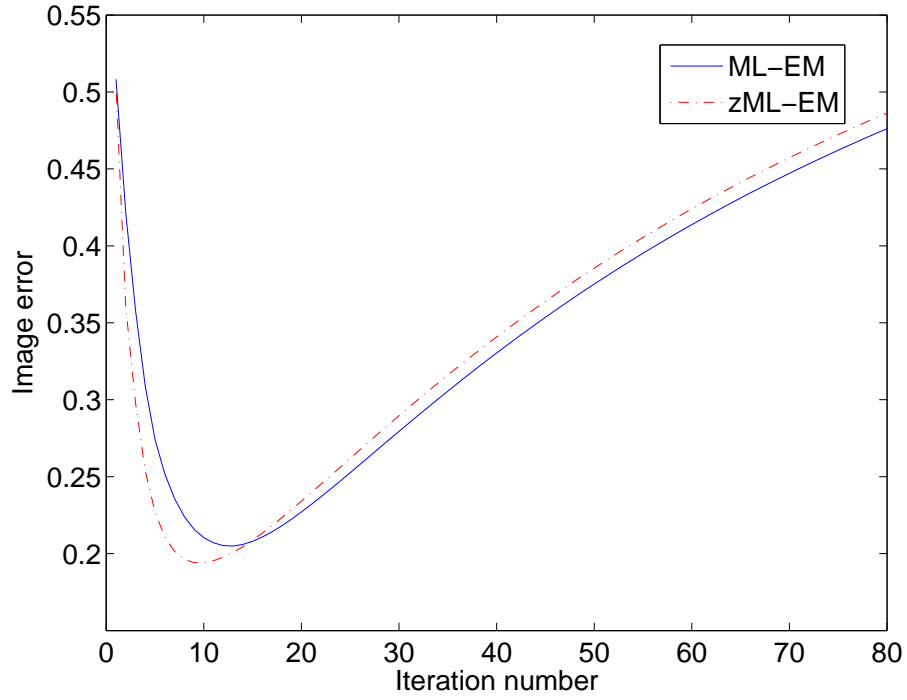
Figure 4.3: Image error plotted as a function of the number of iterations for both ML-EM and zML-EM algorithms.
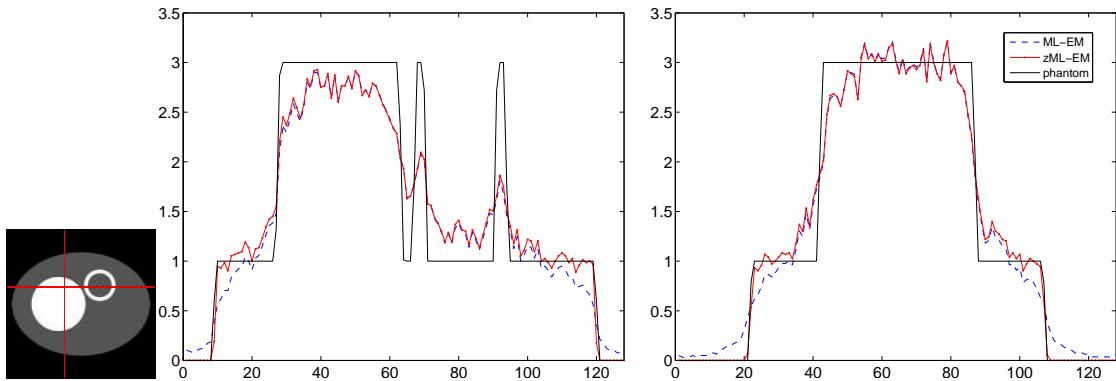
Figure 4.4: The horizontal and vertical profile curves for ML-EM and zML-EM reconstructed images at 6 iterations. The profile positions are indicated in the heart phantom.
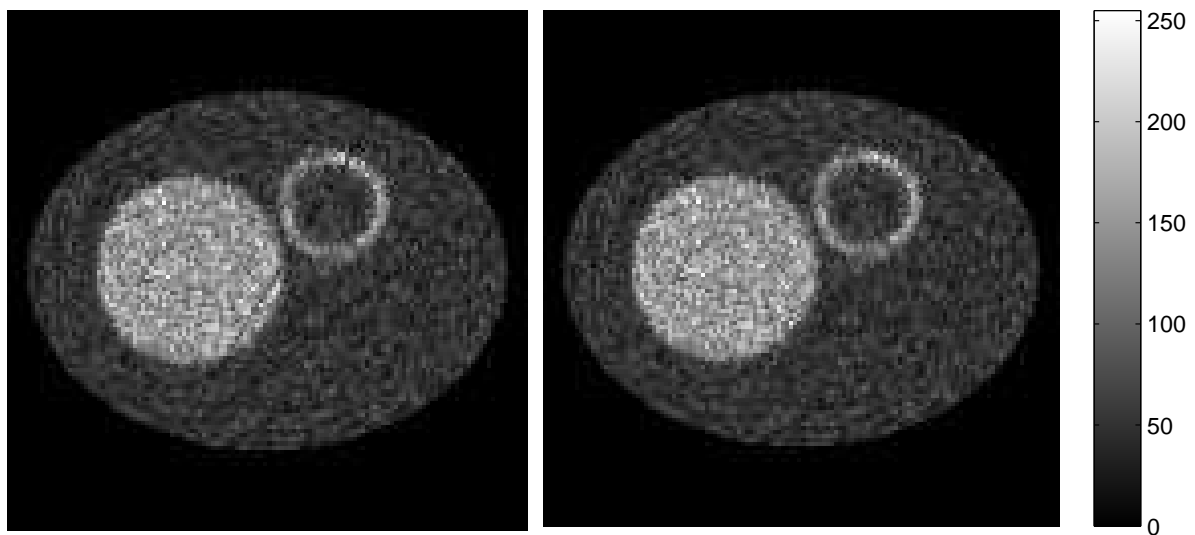
Figure 4.5: The reconstruction results of projections with zero-valued pixels inside using ML-EM (left) and zML-EM (right) algorithms. For the zero-valued pixels inside the projection data, c=0.000001. Thirty iterations were used.

4.6 Discussion and Conclusion

The presented results indicated that the zML-EM algorithm can handle the zero-valued projections properly by varying the c value for different cases, while the conventional ML-EM algorithm generates larger errors in the results. For low count data, the ML-EM algorithm is terminated before it is fully converged in order to maintain the noise level, resulting in a blurred boundary. By introducing a c value that is greater than 1, the boundary in the image is well preserved even at extremely low iterations. With the increase in the iteration number, a smaller c value (still ≥ 1) is suggested. For zero-values inside the object region, black lines are observed in the reconstruction result of the ML-EM algorithm. However, these black lines are completely removed by applying the zML-EM algorithm with a c value that is less than 1, even close to zero.

Based on the computer simulation results above, we could make the following observations:

The weighting strategy of the ML-EM algorithm can be further improved for the zero-valued projections.

(i) When the zero-valued measurement is correct, the weighting in the ML-EM algorithm is too conservative, though the true value is already known.

(ii) When the zero-valued measurement is incorrect, the ML-EM algorithm's weighting "$1/\sum_m a_{im}x_m$" over emphasizes the zero-valued projection at high iterations.

We propose to replace the weighting "$1/\sum_m a_{im}x_m$" by "$c_i/\sum_m a_{im}x_m$".

(i) In regions where the zero-valued measurement is correct, set $c_i > 1$.

(ii) In regions where the zero-valued measurement is incorrect, set $0 \leq c_i < 1$.

(iii) In regions where the projection data are positive, set $c_i = 1$.

In practice, it is fairly easy to determine whether the zero measure is correct or not by examination of its neighboring measurement values.

In conclusion, the new zML-EM method improves the reconstruction results by using an appropriate c value and has a smaller image error than that of the conventional ML-EM at low iterations. As with the conventional ML-EM algorithm, the proposed zML-EM algorithm retains the property of count conservation at every iteration.

4.7 References

[1] L. A. Shepp and Y. Vardi, "Maximum likelihood reconstruction for emission tomography," *IEEE Trans. Med. Imaging*, vol. 1, no. 2, pp. 113–122, 1982.

[2] P. P. Bruyant, "Analytic and iterative reconstruction algorithms in SPECT," *J. Nucl. Med.*, vol. 43, no. 10, pp. 1343–1358, 2002.

[3] D. W. Wilson and B. M. Tsui, "Noise properties of filtered-backprojection and ML-EM reconstructed emission tomographic images," *IEEE Trans. Nucl. Sci.*, vol. 40, no. 4, pp. 1198–1203, 1993.

[4] G. L. Zeng, *Medical Image Reconstruction: A Conceptual Tutorial.* Higher Education Press, 2010.

[5] K. Lange and R. Carson, "EM reconstruction algorithms for emission and transmission tomography," *J. Comput. Assist. Tomog.*, vol. 8, no. 2, pp. 306–316, 1984.

[6] H. H. Barrett, D. W. Wilson, and B. M. Tsui, "Noise properties of the EM algorithm. i. theory," *Phys. Med. Biol.*, vol. 39, no. 5, p. 833, 1994.

CHAPTER 5

GEOMETRIC CALIBRATION AND IMAGE
RECONSTRUCTION FOR SEGMENTED
SLANT BEAM STATIONARY
CARDIAC SPECT SYSTEM

5.1   Abstract

A dedicated stationary cardiac SPECT system is developed with a novel segmented-slant-hole collimator. The goal of this paper is to calibrate this new imaging geometry with a point source. Unlike the commercially available dedicated cardiac SPECT systems, which are specialized and can only be used to image the heart, our proposed cardiac system is based on a conventional SPECT system, but the collimator is replaced with a segmented-slant-hole collimator. For a dual-head SPECT system, two segmented collimators, each with seven sections, are arranged in an L-shaped configuration such that it can produce a complete cardiac SPECT image with only one gantry position. A calibration method is developed to estimate the geometric parameters of each collimator section as well as the detector rotation radius, under the assumption that the point source location is calculated using the central-section data. With a point source located off the rotation axis, geometric parameters for each collimator section can be estimated independently. The parameters estimated individually are further improved by a joint objective function that uses all collimator sections simultaneously and incorporates the collimator symmetry information. Estimation results and images reconstructed from estimated parameters are presented for both simulated as well as real data acquired from a prototype collimator. The calibration accuracy was validated by computer simulations with an error of $\sim 0.1°$ for the slant angles and ~ 1 mm for the rotation radius. Reconstructions on a heart insert phantom did not show any image artifacts of inaccurate geometric parameters. Compared to the detector's intrinsic resolution, the estimation error is small and ignorable. Therefore, the accuracy of the calibration is sufficient for the cardiac SPECT imaging.

5.2   Introduction

Dedicated cardiac Single Photon Emission Computed Tomography (SPECT) systems, based on state-of-the-art detector technologies and specific acquisition geometries, offer ultra-fast scans with high image quality for the detection of Coronary Artery Disease (CAD). Very short acquisition times can be achieved mainly through the use of multidetectors or multicollimators (*e.g.*, pinhole, slant hole) that are oriented from different directions and image the heart simultaneously [1–5]. Adding detectors also adds more parameters to be calibrated. As compared with the conventional parallel-hole system, the cardiac SPECT system with sophisticated collimators is more difficult to calibrate. Knowledge of the precise geometric parameters is essential for accurate image reconstruction.

The optimal method for calibration depends on the scanner geometry. Many geometrical calibration methods have been proposed since the early 1980s [6–10]. For parallel and slant geometry, Busemann *et al.* presented a calibration procedure that entailed measuring a plate containing 16 point sources at two different positions [6]. For fan-beam geometry, a method of minimizing the distance between the experimental measurement and the analytical locations of one point source was proposed by Gullberg *et al.* [7] and was extended to cone beam geometry [8]. A good approximation of initial values was required to avoid unrealistic solutions. More recently, multiple point sources with known relative distances were applied in calibration to eliminate correlation of scanner parameters [9–12]. Although this method only needs coarse initial values, the design of the calibration object requires very high precision.

The aim of this paper is to calibrate a prototype dedicated stationary cardiac SPECT system with segmented-slant-hole collimators. This stationary cardiac SPECT is realized by simply mounting the segmented-slant-hole collimators on the widely-used two-head conventional SPECT system. Each collimator includes seven sub-collimators slanted towards a common volume at the rotation center. With two gamma camera detectors at 90° apart, 14 views are acquired simultaneously. To obtain a high-quality reconstruction, a precise calibration of geometrical parameters is necessary.

This work develops a geometric calibration procedure for the segment-slant-hole stationary cardiac SPECT. Even though our system is able to produce a cardiac image without gantry rotation, we rotate the gantry for 180° for the system calibration procedure. Our method consists of two steps. In the first step, the central sub-section that has the conventional parallel-hole collimator is used to estimate the location of the point source, so that the point source location is known. After the location of the point source is known,

in the second step, the parameter estimation problem becomes a minimization problem with a quadratic objective function. The quadratic nature of the objective function enables closed-form estimation. Parameters for each section are estimated independently. A joint objective function can be set up in the second step, so that all parameter can be estimated simultaneously. The joint objective function can incorporate the collimator symmetry information and makes the estimation more accurate.

This paper is organized as follows. In section 5.3, we briefly introduce the segmented-slant-hole stationary cardiac SPECT system. In section 5.4, we explain the details of the proposed calibration method. Our method has been verified by Monte Carlo simulations and actual system measurements. In Monte Carlo simulations, the ground truth is known. In real data studies, the projections were acquired with a prototype system with a segmented-slant-hole collimator, and then the geometric parameters were estimated. The experiments and results are illustrated in sections 5.5 and 5.6, respectively. Finally, we discuss the results in section 5.7.

5.3   Segmented Slant-Hole Collimator

The proposed segmented slant-hole collimator has 7 segments, as shown in Figure 5.1. Section I is the conventional parallel-hole collimator. Sections II~VII are slant-hole collimators. Within a section, the collimator holes are parallel to each other. The region in front of the collimators, which is "seen" by all sections, is the common volume (CV) centered at the rotation center. The region of interest must be contained in the CV.

Without loss of generality, we use section III to introduce slant angles, as shown in Figure 5.2. The slant angles of each section must be estimated before image reconstruction can be performed. To describe the geometry of the scanner, we introduce two sets of axes: the detector and the object sets of axes. The detector set of axes is defined by (u, v, w), where the u-axis refers to the horizontal axis, the v-axis refers to the vertical axis that is parallel to the rotation axis of the detector, and the w-axis is normal to the detector and oriented toward the rotation axis (see Figure 5.2).

The object is defined in the (x, y, z) system. In this paper, we define the origin of the object system to be at the intersection of the w-axis and the rotation axis, and the rotation axis is referred to as the z-axis. When the detector rotation angle is $\theta = 0°$, the u-axis is parallel to the y-axis.

The transformation from the (x, y, z) coordinate system to the (u, v, w) coordinate system is equivalent to a clockwise rotation about the z-axis by angle θ plus a shift of rotation radius f in the w direction. The final transformation is given by
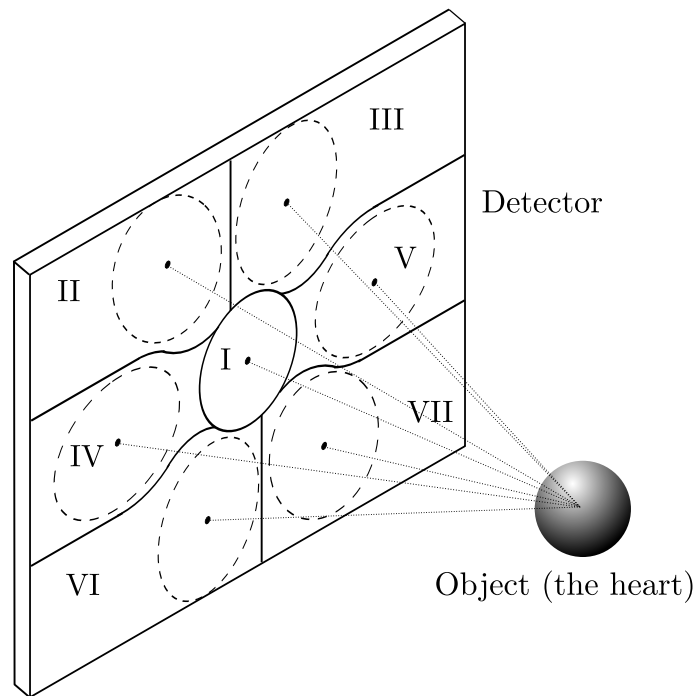
Figure 5.1: Illustration of the proposed 7-segment slant-hole collimator. The projection is elongated at outer sections. Ellipses in dash lines represent the projection on that section of the detector when a sphere is placed at the rotation center.
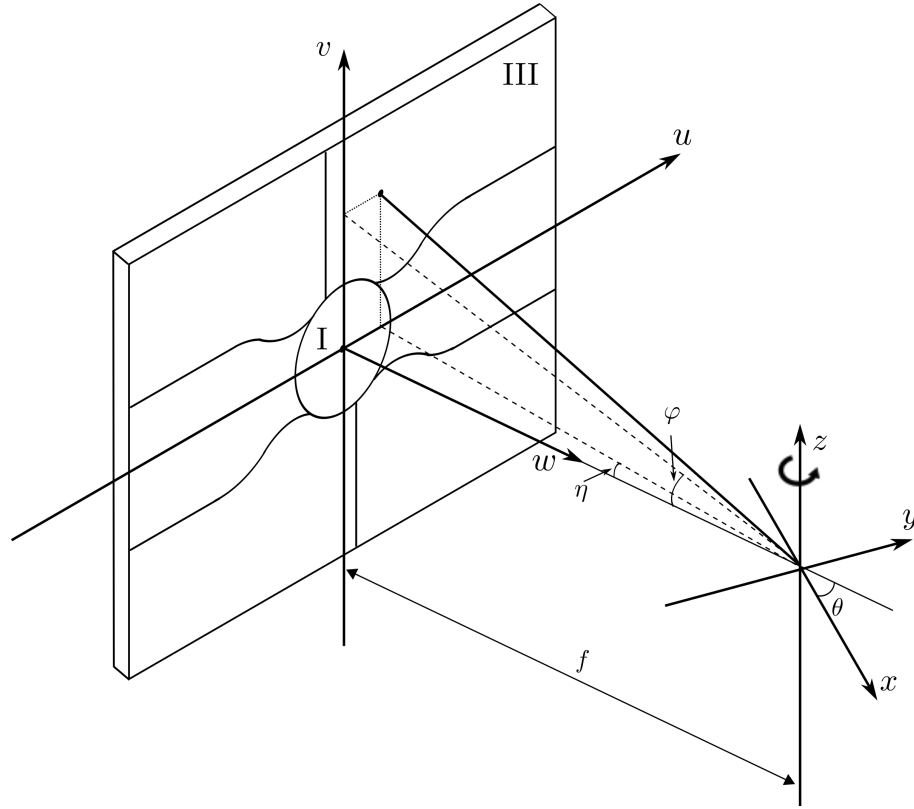
Figure 5.2: Definition of slant angles η and φ, detector coordinates, and object coordinates. The z axis is the rotation axis of the detector.

$$\begin{bmatrix} w \\ u \\ v \end{bmatrix} = \begin{bmatrix} \cos\theta & \sin\theta & 0 \\ -\sin\theta & \cos\theta & 0 \\ 0 & 0 & 1 \end{bmatrix} \begin{bmatrix} x \\ y \\ z \end{bmatrix} + \begin{bmatrix} f \\ 0 \\ 0 \end{bmatrix} = \begin{bmatrix} x\cos\theta + y\sin\theta + f \\ -x\sin\theta + y\cos\theta \\ z \end{bmatrix} \tag{5.1}$$

This paper proposes a method to estimate the slant angles η and φ for each section. The definitions of slant angles η and φ are illustrated in Figure 5.2. The detector rotation radius f will also be estimated. This method uses one point source P at the location (x_0, y_0, z_0) that is away from the rotation axis. Without loss of generality, again, we use section III to show the setup of the point source P relative to the detector, as shown in Figure 5.3. The location of P can be obtained using two or more views from a conventional parallel-hole collimator, for example, section I of our proposed segmented collimator. According to Figure 5.3, the image of point source P in section I has the coordinates

$$(u_{I\theta}, v_{I\theta}) = (-x_0\sin\theta + y_0\cos\theta, z_0) \tag{5.2}$$

and the distance from the point source P to the detector is

$$D_\theta = x_0\cos\theta + y_0\sin\theta + f. \tag{5.3}$$

The image of the point source P in section III is related to $(u_{I\theta}, v_{I\theta})$ as, according to Figure 5.3,

$$u_{III\theta} = u_{I\theta} + D_\theta\tan\eta = (-x_0\sin\theta + y_0\cos\theta) + (x_0\cos\theta + y_0\sin\theta + f)\tan\eta, \tag{5.4}$$

$$v_{III\theta} = v_{I\theta} + D_\theta\tan\varphi = z_0 + (x_0\cos\theta + y_0\sin\theta + f)\tan\varphi. \tag{5.5}$$

In our system, the distance from the rotation axis to the back of the collimator is referred to as the focal length of the collimator (shown in Figure 5.2 and Figure 5.3). Unlike a fan-beam or cone-beam imaging geometry, the focal-length of the segmented slant-hole collimator is decided by the rotation radius and can be altered in the range of CV, even after the collimator is fabricated. Here, we define the center of the detector to be the origin of the (u, v) coordinate system, which is also the center of section I. Therefore, the focal point is the same as the origin of the (x, y, z) coordinate system, and the focal length is the same as the detector rotation radius f. The center coordinates of other outer sections are defined as $(f\tan\eta, f\tan\varphi)$, as shown in Figure 5.2.

5.4   Calibration of Segmented-Slant-Hole Collimator

5.4.1   Independent Estimation of the Parameters

In (5.4) and (5.5), the measurements are $u_{III\theta}$ and $v_{III\theta}$. The point source location is also assumed to be known, because it can be estimated by using the projection data from section I. Thus, the unknowns to be estimated are: $\tan\eta$, $\tan\varphi$, and f.
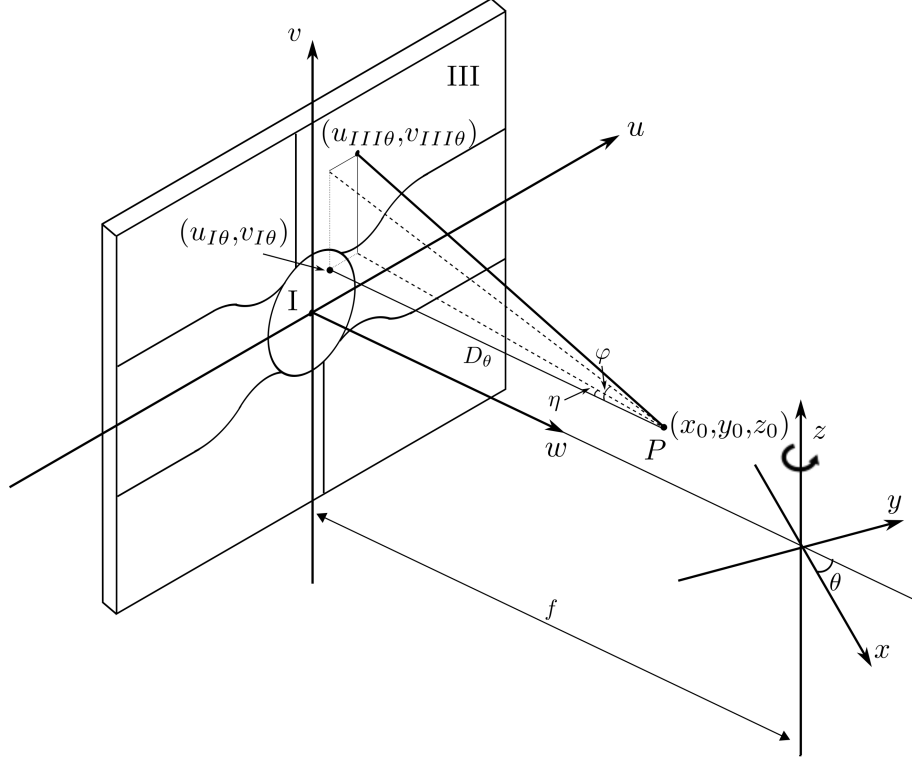
Figure 5.3: The setup of a point source P.

Based on Equations (5.4) and (5.5), the unknowns can be estimated by minimizing the following error functions:

$$E_u = \sum_{\theta} [u_{III\theta} - u_{I\theta} - (x_0 \cos\theta + y_0 \sin\theta + f)\tan\eta]^2, \tag{5.6}$$

$$E_v = \sum_{\theta} [v_{III\theta} - z_0 - (x_0 \cos\theta + y_0 \sin\theta + f)\tan\varphi]^2. \tag{5.7}$$

The error functions (5.6) and (5.7) are the usual quadratic objective functions. This becomes obvious if (5.6) is rewritten as

$$E_u = \sum_{\theta} [u_{III\theta} - u_{I\theta} - (x_0 \cos\theta + y_0 \sin\theta)a - b]^2, \tag{5.8}$$

with the unknown variables defined as

$$a = \tan\eta$$
$$b = f\tan\eta. \tag{5.9}$$

Taking partial derivatives of E_u with respect to a and b, respectively, and setting the partial derivatives to zero, we have

$$\sum_{\theta} [u_{III\theta} - u_{I\theta} - (x_0 \cos\theta + y_0 \sin\theta)a - b](x_0 \cos\theta + y_0 \sin\theta) = 0 \tag{5.10}$$

$$\sum_\theta [u_{III\theta} - u_{I\theta} - (x_0 \cos\theta + y_0 \sin\theta)a - b] = 0, \tag{5.11}$$

that is,

$$\begin{bmatrix} \sum_\theta (x_0 \cos\theta + y_0 \sin\theta)^2 & \sum_\theta (x_0 \cos\theta + y_0 \sin\theta) \\ \sum_\theta (x_0 \cos\theta + y_0 \sin\theta) & \sum_\theta 1 \end{bmatrix} \begin{bmatrix} a \\ b \end{bmatrix}$$
$$= \begin{bmatrix} \sum_\theta [u_{III\theta} - u_{I\theta}](x_0 \cos\theta + y_0 \sin\theta) \\ \sum_\theta [u_{III\theta} - u_{I\theta}] \end{bmatrix}. \tag{5.12}$$

Therefore, the closed-form solutions for a and b are obtained as

$$\begin{bmatrix} a \\ b \end{bmatrix} = \begin{bmatrix} \sum_\theta (x_0 \cos\theta + y_0 \sin\theta)^2 & \sum_\theta (x_0 \cos\theta + y_0 \sin\theta) \\ \sum_\theta (x_0 \cos\theta + y_0 \sin\theta) & \sum_\theta 1 \end{bmatrix}^{-1}$$
$$\begin{bmatrix} \sum_\theta [u_{III\theta} - u_{I\theta}](x_0 \cos\theta + y_0 \sin\theta) \\ \sum_\theta [u_{III\theta} - u_{I\theta}] \end{bmatrix}. \tag{5.13}$$

Note that when $x_0 \neq 0$ and $y_0 \neq 0$, the solution is unique.

The geometrical parameters η and f can be obtained as

$$\eta = \arctan a \tag{5.14}$$
$$f = \frac{b}{a}. \tag{5.15}$$

Similarly, solution for $\tan\varphi$ can be obtained by minimizing (5.7).

5.4.2   Joint Estimation of the Parameters

Notice that parameter f is estimated from both (5.6) and (5.7), and for all outer collimator sections. The outliers can be discarded and the average value of these f values can be used. In fact, to further improve the accuracy of the parameters, a joint objective function using all collimator sections can be set up in (5.18) below. Some extra information can be added to this new joint objective function. For example, the collimator is symmetric. Sections II and VII are mirror symmetric. Sections III and VI are mirror symmetric. Sections IV and V are mirror symmetric. This joint objective function can be further simplified if the point source P can be carefully positioned on the axis of rotation. The mirror symmetry property is able to average and reduce the errors generated in the individual estimation method discussed in section 5.4.1. Let us consider two special cases below.

5.4.2.1   Special Case 1: Using Two Orthogonal Views

We set two detectors at $0°$ and $90°$, respectively, to acquire two high-count (*i.e.*, low noise) projection data of a point source. The location of the point source is given in section

I, as x_0=-$u_{I90°}$, y_0=$u_{I0°}$, z_0=$v_{I0°}$. Thus, (x_0, y_0, z_0) is known. Using two projections at $0°$ and $90°$, expressions of $f \tan \eta$ and $\tan \varphi$ can be derived from Equations (5.4) and (5.5). Take section III as an example:

$$\text{At } 0° \qquad u_{III0°} = y_0 + (x_0 + f) \tan \eta \qquad\qquad (5.16a)$$

$$v_{III0°} = z_0 + (x_0 + f) \tan \varphi \qquad\qquad (5.17a)$$

$$\text{At } 90° \qquad u_{III90°} = -x_0 + (y_0 + f) \tan \eta \qquad\qquad (5.16b)$$

$$v_{III90°} = z_0 + (x_0 + f) \tan \eta \qquad\qquad (5.17b)$$

Combining (5.16a) and (5.16b) yields (5.16) below, and combining (5.17a) and (5.17b) yields (5.17) below:

$$(y_0 - x_0)f \tan \eta = (u_{III0°}y_0 - u_{III90°}x_0) - (x_0^2 + y_0^2) \qquad\qquad (5.16)$$

$$(x_0 - y_0) \tan \varphi = v_{III0°} - v_{III90°}. \qquad\qquad (5.17)$$

A joint objective function is then readily formed by (5.16) and (5.17) by considering all outer sections simultaneously,

$$\sum_{i=II}^{VII}[(y_0 - x_0)f \tan \eta_i - (u_{i0°}y_0 - u_{i90°}x_0) + (x_0^2 + y_0^2)]^2 + \sum_{i=II}^{VII}[(x_0 - y_0) \tan \varphi_i - (v_{i0°} - v_{i90°})]^2$$

$$(5.18)$$

Here, $x_0 \neq y_0$. The collimator is symmetric with respect to the center, we enforce that $\eta_{II} = -\eta_{VII}$, $\eta_{III} = -\eta_{VI}$, $\eta_{IV} = -\eta_V$. Minimizing (5.18) gives all the unknown parameters: f, η_i and φ_i.

5.4.2.2 Special Case 2: Using One View with the Point Source on the Axis of Rotation

If we are able to carefully position the point source on the rotation axis by using the detector L-shaped configuration, the above formulation can be further simplified: $x_0 = y_0 = 0$. When the point source is placed on the rotation axis, the sinogram will be a straight line. We thus can only use one view to estimate the slant angles. Equations (5.4) and (5.5) are reduced to

$$u_{III\theta} = f \tan \eta \qquad\qquad (5.19)$$

$$v_{III\theta} = z_0 + f \tan \varphi, \qquad\qquad (5.20)$$

which only depend on the parameters of the slant-hole geometry. The joint objective function for η_i and φ_i can be readily set up by (5.4) and (5.5) as

$$\sum_{i=II}^{VII}[(f \tan \eta_i - u_i)^2 + (z_0 + f \tan \varphi_i - v_i)^2] \qquad\qquad (5.21)$$

where $(u_i,\ v_i)$ is the projection location of the point source at the ith outer collimator section.

To summarize the estimation procedure, we first use a point source data set with the point source off the axis of rotation and use the data in section I to obtain the point source location $(x_0,\ y_0,\ z_0)$. Second, independent estimation of f, η_i, and φ_i is obtained according to the method in section 5.4.1. Finally, the estimates of f, η_i, and φ_i are used as the initial values and we use the method in section 5.4.2.2 to further refine the estimates.

5.4.3 Geometric Point Response Function for Slant-Hole Collimator

In order to reduce the dead-zone of the slant collimators, the collimator hole-length is chosen to be very short. This results in a low-energy high-sensitivity (LEHS) collimator; thus, geometric-blurring compensation is necessary. The differences between the point response functions (PRS) for the conventional parallel-hole system and the slant-hole system are shown in Figure 5.4. It is observed that the PRF is symmetric for the conventional parallel-hole collimator. However, for the slant-hole collimator, the PRF is asymmetric [13]. The PRF is elongated in the direction of angle β, as shown in Figure 5.5. The tilt angle α and the slant angle β are calculated as

$$\tan\alpha = \frac{\tan\varphi}{\tan\eta}, \tag{5.22}$$

$$\tan\beta = \sqrt{\tan^2\eta + \tan^2\varphi}. \tag{5.23}$$

5.5 Experiments

Experiments were performed using simulated as well as real data acquired from a prototype segmented-slant-hole collimator. The computer simulation experiment evaluated
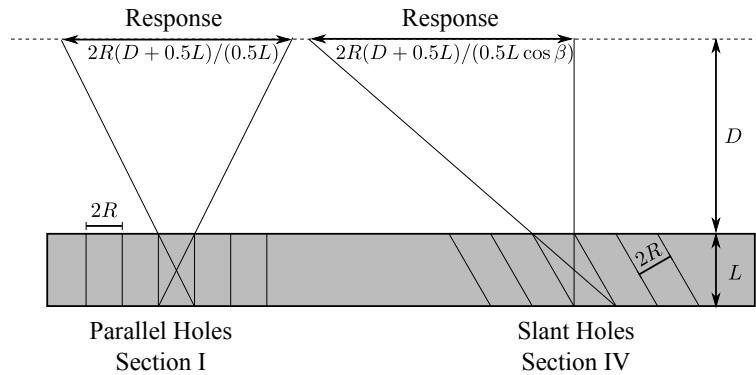
Figure 5.4: Illustration of the geometric response for the parallel holes and slant holes.
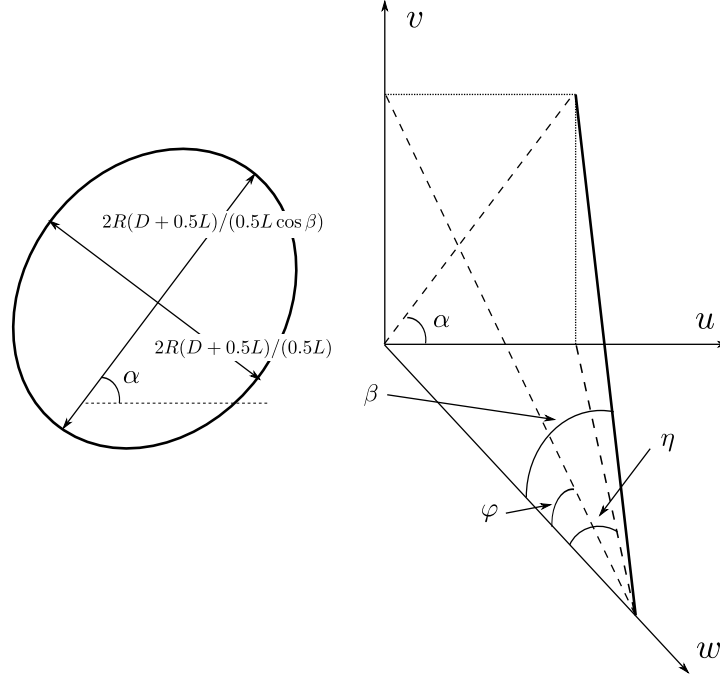
Figure 5.5: A close-up diagram of a point response function's foot print with respect to slant angle α and β.

the calibration accuracy with given parameters. The real-data experiment calibrated the prototype collimator.

5.5.1   Data Generation

To validate the proposed method, we simulated a dual-head SPECT system with the same geometry as that of our prototype system using the GATE (Geant4 Application for Tomographic Emission) Monte Carlo simulation tool [14, 15]. The Monte Carlo scripts are listed in the Appendix 5.9.1. The parameters of the slant holes in Figure 5.3 are given in Table 5.1. The hole diameter is the diameter of the smallest cross section of the hole and the septum length is elongated at outer sections. One point source was placed at (10, 10, 20) (unit: mm) away from the rotation center. The detector rotated in a circular orbit and acquired data every 15° over a range of 180°. Another high-count data set was acquired at 0°, when one point source was placed on the rotation axis. The pixel size of projection matrix was 1.25 mm. As a comparison, the calibration results were applied in the reconstruction of a two-point phantom.

Table 5.1: System parameters

Isotope	^{99m}Tc	Septum length of section II&VII	16.6 mm
Energy window	15%	Septum length of section III&VI	16.22 mm
Hole shape	Hexagon	Septum length of section IV&V	17 mm
Hole diameter (2R)	1.9 mm	Septum length of section I	15 mm
Septal thickness	0.3 mm		

5.5.2   Slant-Hole Collimator Calibration

Our segmented collimator was fabricated by Nuclear Fields (Des Plaines, IL), who provided us some rough estimation of some parameters. Here, we used the proposed method to estimate the collimator parameters. The collimator is mounted on a Siemens E-CAM Signature Series® SPECT camera. Details about the geometry of the collimator are listed in Table 5.1. A point source, which is made of a tiny drop of 100 μCi ^{99m}Tc in a capillary tube, was placed at an arbitrary position that is away from the rotation axis but in the field of view. Images were acquired every 5° over 180° with a total of 21 min study time. For more accurate results, a set of high-count data were acquired at 0° and 90° while keeping the setup of the system constant. The estimated parameters were used to reconstruct the image of the point source and a heart insert with 1.0 m Ci ^{99m}Tc in the heart wall. The projection matrix was 256×256 with a pixel size at 2.3976 mm.

5.6   Results

5.6.1   Validation

The location of the point source estimated from section I is presented in Table 5.2. As can be seen from the table, there is a good agreement between the estimated location and the actual location. The error of estimation is around 0.2 mm and is well below the detector's intrinsic resolution. Based on the location of projected point source, the slant angles η and φ were estimated from each outer section and are presented in Table 5.3. Due to the uncertainties in measuring the center of the projected point source, the value of f varies from 226.1551 mm to 267.0329 mm. A further improvement is necessary to increase the estimation accuracy. Parameters f and η were varied in a range of 10 mm and 1.5° around each mean, respectively. The value 226.1551 mm, which is far from all other estimated f, was discarded. The minimum of the joint objective function was found at parameters listed in Table 5.4. The difference between the estimated and actual value is less than 0.1° for the slant angles and 1 mm for the rotation radius.

Table 5.2: Location of the point source

	Actual value (mm)	Estimated value (mm)
x_0	10	9.7764
y_0	10	9.3445

**Table 5.3**: Individually estimated parameters with a point source off the rotation axis

Section No.	Estimated η (deg)	Estimated f (mm)	Estimated φ (deg)	Estimated f (mm)
II	-27.1997	250.8792	21.9388	266.535
III	13.6601	253.1167	24.8368	261.8161
IV	35.8831	259.7550	7.1090	226.1551
V	-35.7989	260.2545	-6.3202	256.2762
VI	-13.6432	251.7194	-24.8489	261.8941
VII	25.743	267.0329	-21.9859	265.1175
f (mm)	256.6293 ± 11.0953			

Table 5.4: Jointly estimated parameters, giving improved results

Section No.	Actual η (deg)	Actual φ (deg)	Actual f (mm)	Improved η (deg)	Improved φ (deg)	Improved f (mm)
II	-25.7143	21.9976	266.5	-25.8	22.0737	265.5
III	12.8571	24.5452	266.5	12.9	24.6198	265.5
IV	35	6.0963	266.5	35.1	6.1188	265.5
V	-35	-6.0963	266.5	-35.1	-6.1188	265.5
VI	-12.8571	-24.5452	266.5	-12.9	-24.6198	265.5
VII	25.7143	-21.9976	266.5	25.8	-22.0737	265.5

Figure 5.6 shows the reconstruction results with estimated parameters before and after blurring correction. The shape of the point source is well reconstructed without any distortion. As a comparison, we also performed the reconstruction with true parameters. The reconstruction results of two point sources from estimated parameters and true parameters are displayed in Figure 5.7. No significant difference is observed in these two images.
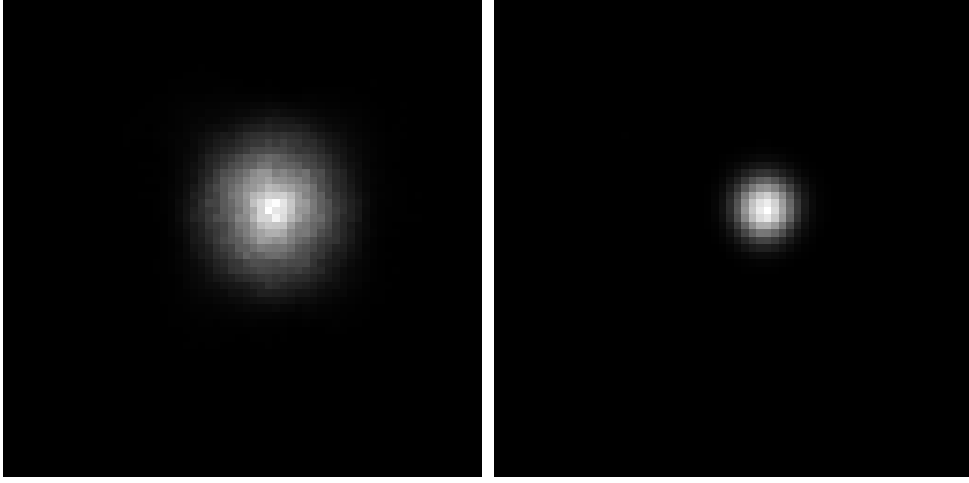
Figure 5.6: Reconstruction results of a point source without (left figure) and with (right figure) blurring correction. Five iterations and 50 iterations were used, respectively.
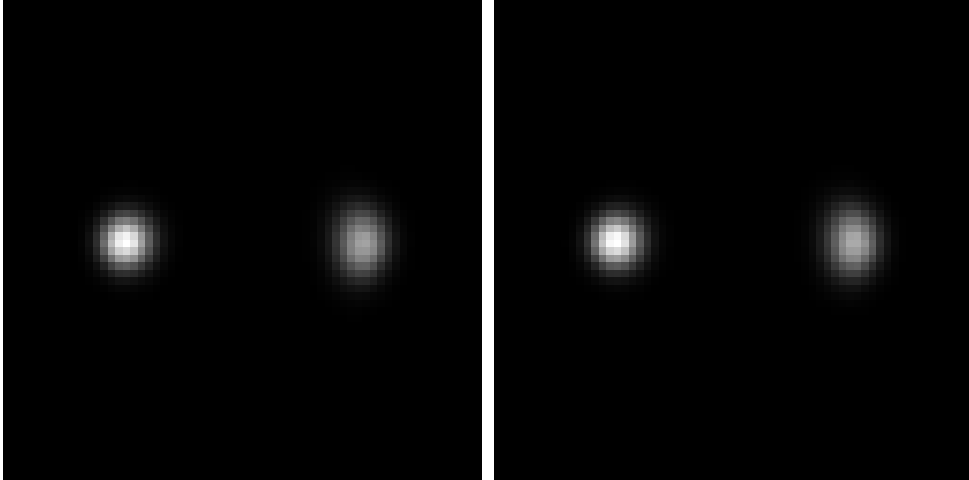

Figure 5.7: Reconstruction results of two point sources at 50 iterations. The left one was reconstructed with actual parameters. The right one was reconstructed with estimated parameters.

5.6.2 Slant-Hole Collimator Calibration

The projection of a point source is shown in Figure 5.8. As is seen, the point source is elongated at outer sections along the slant angle. Table 5.5 lists the calibrated slant-hole parameters for each section. The location of the point source estimated from the central sub-detector is at x_0 =-2.1605 mm, y_0 =42.5028 mm. Images reconstructed with estimated parameters are shown in Figure 5.9. No obvious errors or artifacts from geometric calibration are observed in the point source reconstruction image. The asymmetry in the x-axis and y-axis cuts mainly attribute to the cylinder shape of the capillary tube with 1.0 mm diameter and about 2.0 mm axis height.

The calibrated parameters were further evaluated using the cardiac insert phantom. Figure 5.10 shows the projection image of the heart phantom acquired by the stationary segmented slant beam cardiac SPECT system. In total, 14 projection images were acquired simultaneously. With a resolution compensation, the "U" shape of the heart is well preserved (Figure 5.11). The low contrast and nonuniformity may be caused by the limited view angles.
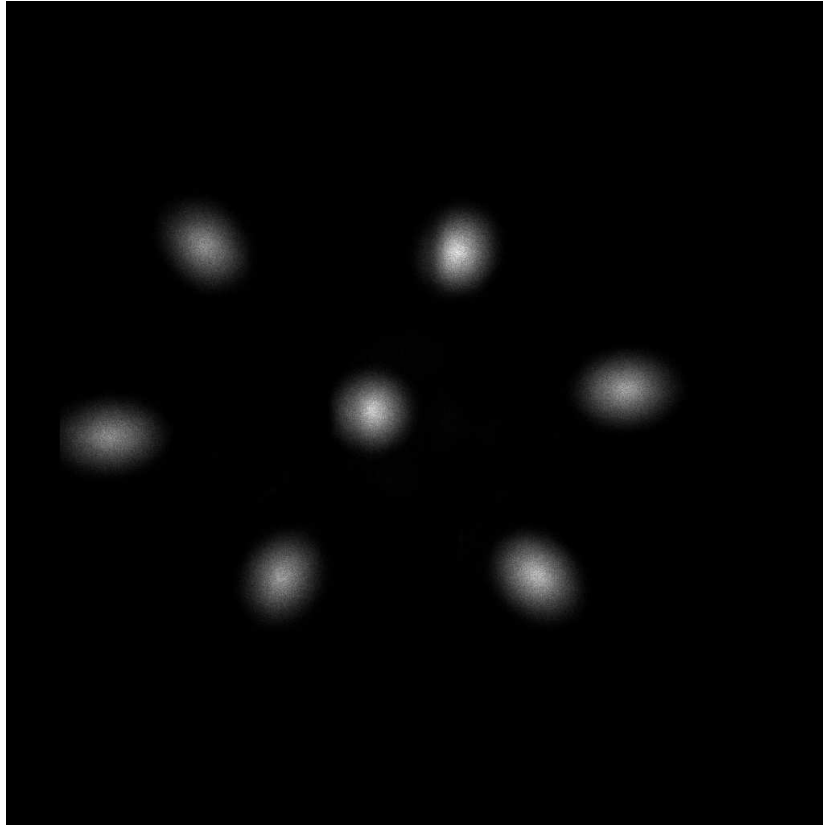
Figure 5.8: The projection of a point source at 90°.

Table 5.5: Parameters for segmented-slant-hole collimator obtained from calibration

Section No.	Estimated η (deg)	Estimated f (mm)	Estimated φ (deg)	Estimated f (mm)	Improved η (deg)	Improved φ (deg)	Improved f (mm)
II	-24.5704	285.484	29.3020	239.1922	-28.1	28.1	249.2
III	17.6198	233.092	29.2392	242.2959	16.1	27.6704	249.2
IV	42.1965	240.394	5.1924	245.6745	39.6	4.4006	249.2
V	-38.7337	253.905	-3.7202	254.9959	-39.6	-4.4006	249.2
VI	-14.7862	257.088	-28.1511	224.7458	-16.1	-27.6704	249.2
VII	29.7619	239.6518	-29.1448	228.0522	28.1	-28.1	249.2
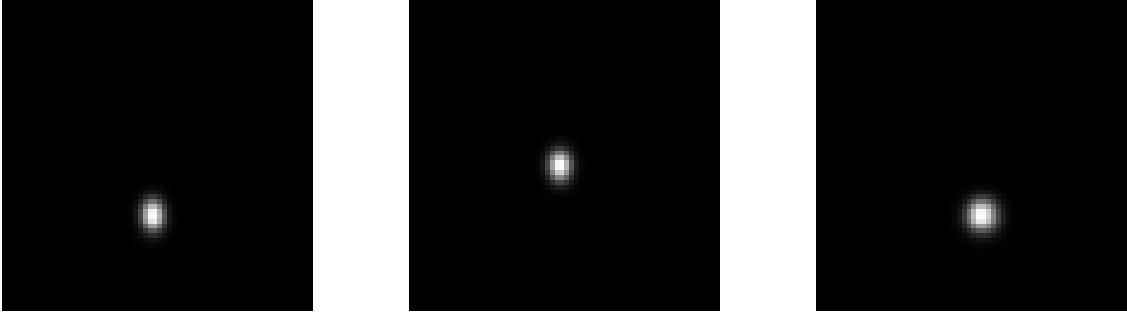
Figure 5.9: The reconstruction results of a point source with improved parameters. From left to right: x-axis, y-axis and z-axis cuts through the point center. 60 iterations were applied.
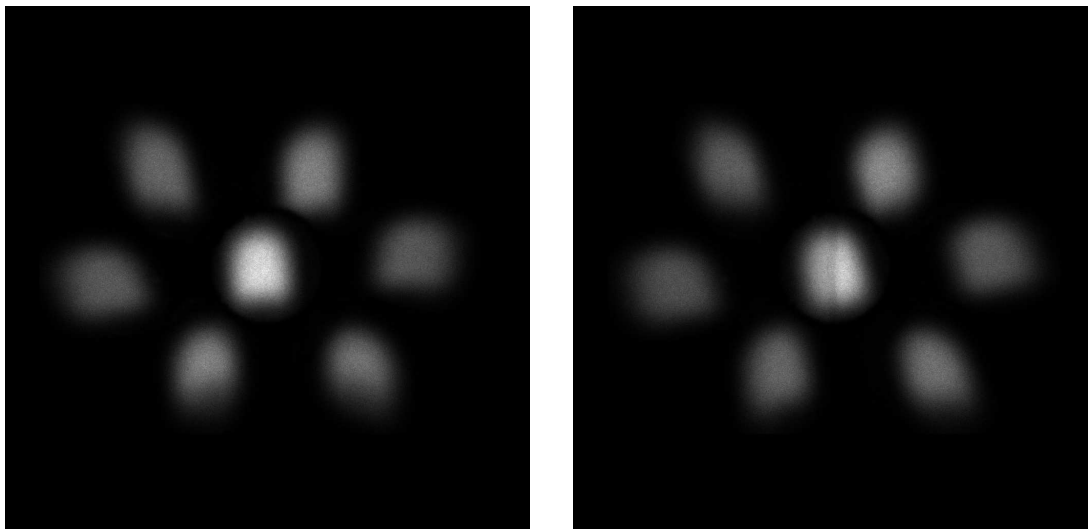
Figure 5.10: The projection of the heart phantom at 0° and 90°.
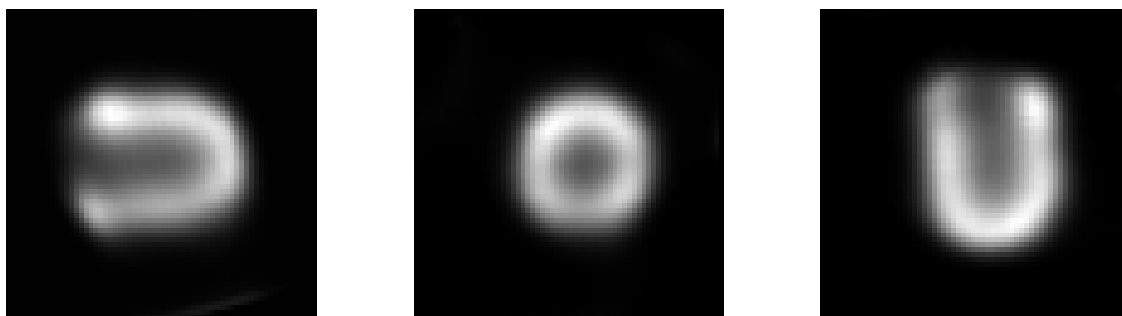
Figure 5.11: The reconstruction results of the heart phantom. From left to right: vertical long-axis (VLA), short-axis (SA), and horizontal long-axis (HLA) cuts.

5.7   Discussion and Conclusions

In this work, a geometrical calibration method was developed for stationary cardiac SPECT with a segmented-slant-hole collimator. The proposed estimation method does not require good initial values or iteration. Also, no precise measurement of point location is required as the point source can be placed at an arbitrary position. The method was validated in computer simulations, which show 0.1° error for slant angle and 1 mm for the rotation radius. It was also successfully applied to a prototype segmented-slant-hole collimator. Errors in the calibration depend on the accurate measurement of the point projection locations, which are limited by data pixel size and noise. For better calibration results, the pixel size is set as small as possible.

5.8   Acknowledgments

5.9   Appendix

5.9.1   Appendix A: Monte Carlo Simulation Code for Slant Hole

Monte Carlo code for parallel hole:

```
/gate/collimator/daughters/name hole
/gate/collimator/daughters/insert hexagone
/gate/hole/geometry/setHeight 15. mm
/gate/hole/geometry/setRadius .95 mm
/gate/hole/placement/setRotationAxis 0 1 0
/gate/hole/placement/setRotationAngle 90 deg
```

The slant hole is constructed by four parallelepiped. For slant-hole collimator, the above code is replaced by following part:

```
/gate/collimator/daughters/name hole
/gate/collimator/daughters/insert parallelepiped
/gate/hole/geometry/setDx 1.097 mm
/gate/hole/geometry/setDy 0.95 mm
/gate/hole/geometry/setDz 15. mm
/gate/hole/geometry/setAlpha 30. deg
/gate/hole/geometry/setTheta 35.3102 deg
```

/gate/hole/geometry/setPhi 261.3274 deg

/gate/hole/placement/setRotationAxis 0 1 0

/gate/hole/placement/setRotationAngle 90. deg

/gate/hole/placement/setTranslation 0. 0.475 0.2742 mm

/gate/collimator/daughters/name hole2

/gate/collimator/daughters/insert parallelepiped

/gate/hole2/geometry/setDx 1.097 mm

/gate/hole2/geometry/setDy 0.95 mm

/gate/hole2/geometry/setDz 15. mm

/gate/hole2/geometry/setAlpha -30. deg

/gate/hole2/geometry/setTheta 35.3102 deg

/gate/hole2/geometry/setPhi 261.3274 deg

/gate/hole2/placement/setRotationAxis 0 1 0

/gate/hole2/placement/setRotationAngle 90. deg

/gate/hole2/placement/setTranslation 0. -0.475 0.2742 mm

/gate/collimator/daughters/name hole3

/gate/collimator/daughters/insert parallelepiped

/gate/hole3/geometry/setDx 1.097 mm

/gate/hole3/geometry/setDy 0.95 mm

/gate/hole3/geometry/setDz 15. mm

/gate/hole3/geometry/setAlpha -30. deg

/gate/hole3/geometry/setTheta 35.3102 deg

/gate/hole3/geometry/setPhi 261.3274 deg

/gate/hole3/placement/setRotationAxis 0 1 0

/gate/hole3/placement/setRotationAngle 90. deg

/gate/hole3/placement/setTranslation 0. 0.475 -0.2742 mm

/gate/collimator/daughters/name hole4

/gate/collimator/daughters/insert parallelepiped

/gate/hole4/geometry/setDx 1.097 mm

/gate/hole4/geometry/setDy 0.95 mm

/gate/hole4/geometry/setDz 15. mm

/gate/hole4/geometry/setAlpha 30. deg

/gate/hole4/geometry/setTheta 35.3102 deg

/gate/hole4/geometry/setPhi 261.3274 deg

/gate/hole4/placement/setRotationAxis 0 1 0

/gate/hole4/placement/setRotationAngle 90. deg

/gate/hole4/placement/setTranslation 0. -0.475 -0.2742 mm

5.10   References

[1] H. Babla, C. Bai, and R. Conwell, "A triple-head solid state camera for cardiac single photon emission tomography (SPECT)," in *Proceddings of SPIE*, vol. 6319, 2006, p. 63190M.

[2] T. Funk, D. L. Kirch, J. E. Koss, E. Botvinick, and B. H. Hasegawa, "A novel approach to multipinhole SPECT for myocardial perfusion imaging," *J. Nucl. Med.*, vol. 47, no. 4, pp. 595–602, 2006.

[3] P. P. Steele, D. L. Kirch, and J. E. Koss, "Comparison of simultaneous dual-isotope multipinhole SPECT with rotational SPECT in a group of patients with coronary artery disease," *J. Nucl. Med.*, vol. 49, no. 7, pp. 1080–1089, 2008.

[4] K. Erlandsson, K. Kacperski, D. Van Gramberg, and B. F. Hutton, "Performance evaluation of D-SPECT: a novel SPECT system for nuclear cardiology," *Phys. Med. Biol.*, vol. 54, no. 9, p. 2635, 2009.

[5] M. Bocher, I. M. Blevis, L. Tsukerman, Y. Shrem, G. Kovalski, and L. Volokh, "A fast cardiac gamma camera with dynamic SPECT capabilities: design, system validation and future potential," *Eur. J. Nucl. Med. Mol. Imag.*, vol. 37, no. 10, pp. 1887–1902, 2010.

[6] E. Busemann-Sokole, "Measurement of collimator hole angulation and camera head tilt for slant and parallel hole collimators used in SPECT," *J. Nucl. Med.*, vol. 28, no. 10, pp. 1592–1598, 1987.

[7] G. T. Gullberg, B. M. Tsui, C. R. Crawford, and E. R. Edgerton, "Estimation of geometrical parameters for fan beam tomography," *Phys. Med. Biol.*, vol. 32, no. 12, p. 1581, 1987.

[8] G. T. Gullberg, B. M. Tsui, C. R. Crawford, J. G. Ballard, and J. T. Hagius, "Estimation of geometrical parameters and collimator evaluation for cone beam tomography," *Med. Phys.*, vol. 17, no. 2, pp. 264–272, 1990.

[9] P. Rizo, P. Grangeat, and R. Guillemaud, "Geometric calibration method for multiple-head cone-beam SPECT system," *IEEE Trans. Nucl. Sci.*, vol. 41, no. 6, pp. 2748–2757, 1994.

[10] Y. Hsieh, G. Zeng, G. Gullberg, and H. Morgan, "A method for estimating the parameters of a fan-beam and cone-beam SPECT system using five point sources,"

J. Nucl. Med., vol. 34, no. 5, pp. p–191p, 1993.

[11] D. Bequé, J. Nuyts, G. Bormans, P. Suetens, and P. Dupont, "Characterization of pinhole SPECT acquisition geometry," *IEEE Trans. Med. Imaging*, vol. 22, no. 5, pp. 599–612, 2003.

[12] D. Bequé, J. Nuyts, P. Suetens, and G. Bormans, "Optimization of geometrical calibration in pinhole SPECT," *IEEE Trans. Med. Imaging*, vol. 24, no. 2, pp. 180–190, 2005.

[13] G. Bal, R. Clackdoyle, G. Zeng, and D. Kadrmas, "Three-dimensional geometric point response correction in rotating slant-hole (RSH) SPECT," in *Nuclear Science Symposium, 1999. IEEE*, vol. 3, 1999, pp. 1423–1427.

[14] D. Strulab, G. Santin, D. Lazaro, V. Breton, and C. Morel, "GATE (Geant4 Application for Tomographic Emission): a PET/SPECT general-purpose simulation platform," *Nucl. Phys. B (Proc. Suppl.)*, vol. 125, pp. 75–79, 2003.

[15] S. Jan, G. Santin, D. Strul, S. Staelens, K. Assie, D. Autret, S. Avner, R. Barbier, M. Bardies, P. M. Bloomfield *et al.*, "GATE: a simulation toolkit for PET and SPECT," *Phys. Med. Biol.*, vol. 49, no. 19, p. 4543, 2004.

CHAPTER 6

SUMMARY AND PERSPECTIVES

6.1   Scientific Contributions

This dissertation is focused on the investigation of a dedicated stationary cardiac SPECT system. This high-sensitivity, ultra-fast and fully stationary SPECT imaging approach consists of an inexpensive and simple modification that can be used on existing dual-head SPECT systems. By replacing the regular collimator with a segmented slant-hole collimator proposed in Chapter 2, each detector is able to acquire 7 view-angles simultaneously, providing a 6-fold gain in sensitivity, compared with a regular low-energy high-resolution SPECT collimator if same spatial resolution is assumed. Notwithstanding, the limited angular sampling and background truncation issues must be carefully evaluated and settled. System parameters, such as the slant angles for each collimator section and rotation radius, must be calibrated accurately in order to obtain an accurate and artifact-free reconstruction.

Computer simulation results in Chapter 3 show that the effect of truncation on the reconstruction is negligible when the number of views is sufficient. For a small number of projections, such as 14 views, the presence of bias and streak artifacts associated with small FOV cause distortion in the reconstruction. This dissertation extends the conventional ML-EM algorithm to the reconstruction of truncated projections with few view angles. To suppress the streak artifacts, the projection array is expanded to match the size of a virtual detector that can measure truncation-free projections. For expanded projection data, the ratios are set to 1 before backprojection. The array extension does not change the value of measured projection data, but reduces the step size of pixels outside the FOV. Therefore, the iterative algorithm is more stabilized. The streak artifacts outside the FOV are significantly suppressed, which in turn reduces image distortion in the FOV.

In low count imaging, there is a probability that a zero-valued projection is acquired during measurement or after preprocessing. When the conventional ML-EM algorithm is close to convergence, the line-integral of the image associated with the wrong zero-valued projection will drive all image pixels along this particular line to zero. This dissertation

introduces a positive constant weighting factor c to zero-valued projections in the ML-EM algorithm in Chapter 4. Computer simulations confirm that applying $c > 1$ for these zero measurements outside the radiation body, the pixels at the background can converge to zero quickly at very low iterations, generating a sharp boundary of the heart phantom. For these zero measurements inside the projection of the radiation body, the black lines are completely removed by setting $c < 1$. Consequently, applying an appropriate weighting for zero-valued projections can result in a smaller image error than that of the conventional ML-EM algorithm.

In Chapter 5, this dissertation also develops a novel calibration method for a prototype segmented slant-hole stationary cardiac SPECT. The geometric parameters for each collimator section are estimated independently first, and then are further improved by a joint objective function that uses all collimator sections and incorporates the collimator symmetry information. In computer simulations, the estimation error of the proposed calibration method is well below the detector's intrinsic resolution. When it is implemented to the prototype cardiac SPECT system using segmented slant-hole collimators, the diameter of the image reconstructed from estimated parameters is almost the same as the actual size of the point source.

6.2 Future Work

This dissertation is an initial study of the segmented slant-hole stationary cardiac SPECT system, focusing on collimator evaluation, image reconstruction of truncated data, and system calibration. Current research does not consider cardiac motion. The size of the heart varies during diastole and systole. The effects of cardiac motion to the size of the common FOV has to be carefully evaluated in the future.

The task of the cardiac SPECT is to detect lesions. Additional task-dependent evaluation methods to assess image quality are needed when the optimized collimator is fabricated. Observer studies and receiver operating characteristics (ROC) analyses are commonly used for image quality assessment [1–7]. The results of observer studies are closely related to clinical applications, so the evaluations will be more convictive. In the observer studies, the proposed segmented-parallel-beam stationary system will be compared with the conventional SPECT system, as well as the multipinhole system at the same scanning time. The Jaszczak torso/heart phantom with attachments can be used to simulate male and female patients. Various lesion sizes, locations, and noise levels can be applied to simulate the real situations. Images with one lesion (positive images) or without lesions (negative

images) will be given to trained observers, who will be asked to indicate whether a lesion is present or absent in each image, as well as where it is and his or her confidence level for the presence of lesions. ROC curves will be generated according to observers' scores. An alternative way is to use channelized Hotelling observer (CHO), which models human observer performance by computers [8–10].

The tailored ML-EM algorithm proposed in Chapter 3 does not consider attenuation and geometric blurring compensation, which are required by accurate quantification. There are two ways to obtain the attenuation map: one is to use X-ray CT and the other is to acquire the attenuation map from the stationary cardiac system. The latter is a big challenge, because the transmission data are both truncated and highly under sampled. How to correct for the attenuation in a stationary cardiac system remains an open problem.

The stationary cardiac SPECT system has big advantages of eliminating the detector motion artifacts and giving time consistent angular data, which is ideal for myocardial perfusion imaging. Furthermore, a dedicated stationary cardiac SPECT will enhance patient comfort by reducing the scanning time. The realization of a fully stationary cardiac SPECT system requires only a simple collimator exchange, which is a common procedure in SPECT imaging rooms. Compared with buying an entire dedicated cardiac SPECT system, the cost of our stationary cardiac SPECT is as low as that of a regular collimator. Most importantly, our segmented parallel-hole collimator allows the SPECT system to obtain 14 images on two detectors and has an approximate 34-fold sensitivity gain in total over a conventional single-head system, while the multipinhole system only has a 2- to 5-fold gain. This dissertation provides solutions to the major problems in a stationary cardiac SPECT system. Further efforts to improve image quality and reduce scan time are still needed.

6.3   References

[1] C. E. Metz, "Basic principles of ROC analysis," in *Seminars in nuclear medicine*, vol. 8, pp. 283–298, Elsevier, 1978.

[2] C. E. Metz, "ROC methodology in radiologic imaging," *Investigative Radiol.*, vol. 21, no. 9, pp. 720–733, 1986.

[3] H. E. Rockette, D. Gur, and C. E. Metz, "The use of continuous and discrete confidence judgments in receiver operating characteristic studies of diagnostic imaging techniques," *Investigative Radiol.*, vol. 27, no. 2, pp. 169–172, 1992.

[4] J. Rolland and H. H. Barrett, "Effect of random background inhomogeneity on observer detection performance," *JOSA A*, vol. 9, no. 5, pp. 649–658, 1992.

[5] H. H. Barrett, J. Yao, J. P. Rolland, and K. J. Myers, "Model observers for assessment

of image quality," *Proc. Natl. Acad. Sci.*, vol. 90, no. 21, pp. 9758–9765, 1993.

[6] B. M. Tsui, J. A. Terry, and G. T. Gullberg, "Evaluation of cardiac cone-beam single photon emission computed tomography using observer performance experiments and receiver operating characteristic analysis," *Investigative Radiol.*, vol. 28, no. 12, pp. 1101–1112, 1993.

[7] G. K. Gregoriou, B. M. Tsui, and G. T. Gullberg, "Effect of truncated projections on defect detection in attenuation-compensated fanbeam cardiac SPECT," *J. Nucl. Med.*, vol. 39, no. 1, pp. 166–175, 1998.

[8] K. J. Myers and H. H. Barrett, "Addition of a channel mechanism to the ideal-observer model," *JOSA A*, vol. 4, no. 12, pp. 2447–2457, 1987.

[9] P. Bonetto, J. Qi, and R. M. Leahy, "Covariance approximation for fast and accurate computation of channelized hotelling observer statistics," *IEEE Trans. Nucl. Sci.*, vol. 47, no. 4, pp. 1567–1572, 2000.

[10] G. L. Zeng and G. T. Gullberg, "A channelized-hotelling-trace collimator design method based on reconstruction rather than projections," *IEEE Trans. Nucl. Sci.*, vol. 49, no. 5, pp. 2155–2158, 2002.